Investigation of the chatter and squeal phenomenon in bicycle disc brakes

Ajaypal Singh

August 2022
TU Delft

REMMENTEST BRAKE TEST

TU Delft

Investigation of the chatter and squeal phenomenon in bicycle disc brakes

by

Ajaypal Singh

to obtain the degree of Master of Science
at the Delft University of Technology,
to be defended publicly on Monday August 22, 2022 at 2:00 PM.

Student number:	5227275	
Project duration:	January 1, 2022 – August 22, 2022	
Thesis committee:	Prof. dr. J. K. Moore, TU Delft ,	Supervisor
	Prof. dr. ir. P. Breedveld, TU Delft ,	Thesis committee Member
	Dr. A. Dressel, TU Delft ,	Thesis committee Member
	Ir. H. Vreman, Koninklijke Gazelle ,	Supervisor
	Ir. S. Heida, Koninklijke Gazelle ,	Thesis committee Member

This thesis is confidential and cannot be made public until August 22, 2024.

An electronic version of this thesis is available at `http://repository.tudelft.nl/`.

Abstract

Bicycle disc brake noise and vibration, which usually falls in the frequency range of 0-2 kHz, is a principal braking quality attribute that has started to attract significant interest from bicycle manufacturers. Brake noise is an irritant to their customers, who see it as a symptom of a defective brake and that leads to unnecessary warranty claims.

Over the years various theories (e.g. stick-slip, sprag-slip, modal coupling) have been developed that explain the noise and vibration generation mechanism in the frictional brakes. Traditionally, research groups working on this issue have conducted their investigations by combining analytical and experimental studies. Likewise, this report aims to predict the brake noise using finite element analysis where the experimental data validates the finite element model.

In order to reproduce the brake noise in the laboratory setting, the brake test machine at the Koninklijke Gazelle laboratory was used. This novel test bench made it possible to run the experiments on the actual bike by providing features to control the bike speed, brake pressure, and weather conditions within the setup. The dynamic characteristics of the brake system were captured with the microphone and the laser Doppler vibrometer. It was established from the results of the brake noise audio and the vibrometer scans that the entire bike vibrated at three peak frequencies during the brake noise events. Brake noise level as loud as 95 decibels was captured. Stick-slip as one of the friction-induced instabilities was identified during the experiments.

Furthermore, a detailed finite element model of the disc brake assembly was developed. Modal analysis on the components of the assembly and a pre-stressed modal analysis on the entire brake assembly was performed. The finite element results compared well with the experimental results. It was observed that there exists doublet modes and intermediate modal coupling in the system.

Limiting the rotor symmetry by adding weights on the rotor ribs was shown to be effective in reducing instabilities. Other ways to counter brake noise by increasing the rotor mass and by introducing a parallel slot in the brake pad were successfully tested.

Contents

1 Introduction 1

2 Background 3

2.1 Stick-slip . . . 3
2.2 Sprag-slip . . . 4
2.3 Mode lock-in . . . 5
2.4 Doublet modes . . . 6
2.5 Stick-slip and Modal coupling . . . 6
2.6 Energy Balance . . . 6

3 Experimental Investigation into Brake Noise 9

3.1 Description of the test bench . . . 9
    3.1.1 Brake test machine . . . 9
    3.1.2 Bicycle components . . . 9
    3.1.3 Data acquisition . . . 10
3.2 Test procedure . . . 13
    3.2.1 Bed-in process . . . 14
    3.2.2 Warm-up process . . . 14
    3.2.3 Test runs . . . 15

4 Experimental Results 17

4.1 Audio Scan results . . . 17
4.2 Vibrometer Results . . . 18
4.3 Investigation into the randomness of brake noise . . . 20
4.4 Discussion . . . 21

5 Finite Element Simulations 25

5.1 Pre-stressed Modal Analysis . . . 25
5.2 Method of Analysis . . . 25
5.3 Limitations of Analysis . . . 26
    5.3.1 Reduced Model . . . 26
    5.3.2 Limited degrees of freedom . . . 26
    5.3.3 Absence of frictional heating . . . 28
    5.3.4 No stick-slip . . . 28
5.4 Development of Finite Element Model . . . 28
5.5 Finite Element Contact Analysis . . . 29
5.6 Modal Analysis . . . 30
5.7 Summary . . . 31

6 Finite Element Simulation Results 33

6.1 Modal analysis of the individual components . . . 33
    6.1.1 Brake pad . . . 33
    6.1.2 Rotor . . . 33
    6.1.3 Summary . . . 35
6.2 Pre-stressed modal analysis of the disc brake assembly . . . 36
6.3 Comparison with the experimental Results . . . 38

7 Countermeasures 43
7.1 Experimental Analysis . . . 43
7.1.1 Reference run . . . 44
7.1.2 Parallel slot in the brake pad . . . 45
7.1.3 Symmetric loading . . . 46
7.1.4 Asymmetric loading . . . 47
7.2 Finite Element Analysis . . . 48
7.2.1 Asymmetric loading . . . 48
7.2.2 Symmetric loading . . . 49
7.3 Summary . . . 50

8 Conclusion and Future Recommendations 53
8.1 Future Work . . . 54
8.2 Final Remarks . . . 54

A Matlab Script 57

B Audio Amplitude Vs. Frequency Plots 59

C Vibrometer Magnitude Vs. Frequency Plots 63

D Derivation of stress matrix in the stiffness matrix 69

1

Introduction

As the number of components on the modern-day bicycles have increased they have become more complex; the e-bikes that are in use today usually run at a higher speed and demand higher power from their braking system. Over the years, bicycle frames have become lighter, and more and more research is being done to reduce the weight even further. Increased friction coefficient as a result of high braking power demand and lighter bicycle frames has resulted in an increase in friction-induced vibrations and noise. The brake noise and vibrations are usually described by a wider array of terminology. Squeal, judder, groan, squeak, and moan are a few of the names found in the literature. There exists no precise definition of these noises and various automobile manufacturers have devised their own nomenclatures to classify the brake noise. Adnan Akay [4] provided a classification of the brake noise based on their frequency of vibration (see Figure 1.1), which is widely accepted by his peers and the industry alike.

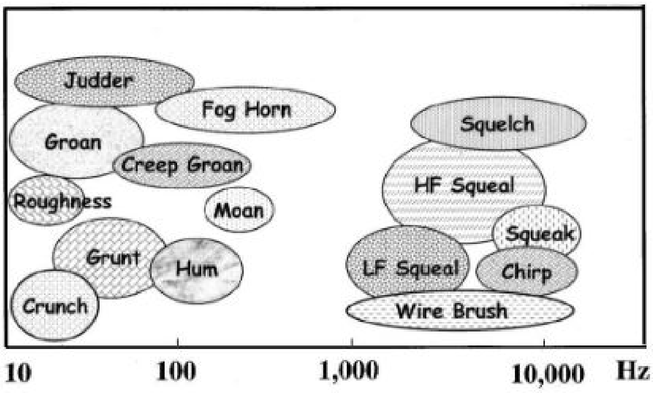

Figure 1.1: Automobile brake noise classification by Adnan Akay based on the frequency of vibration [4]

The classification by Adnan Akay is for the brake noise in automobiles. However, the bikes have a completely different frequency spectrum of the brake noises and thus the automobile brake noise frequency spectrum is not entirely valid for the bicycle brake noises. Therefore, in this report, the frequency range of 550-650 Hz is classified as chatter, 1100-1250 Hz is classified as a squeal, and 1750-1850 Hz is classified as a high-frequency squeal.

Brake noise has obvious environmental issues since they add to noise pollution. It is known that the human ear is the most sensitive in the frequency range of 1-4 kHz, therefore, the squeal and high-frequency squeal cause the most amount of annoyance to the rider and the bystanders [21]. Besides environmental issues, brake noise affects the brake and bicycle manufacturers adversely. The brake manufacturers spend around 50% of their R&D budget on the brake noise and vibration issues, and these issues are responsible for more than half of their after-sales service expenses [2]. The brake manufacturers suffer from economic penalties because of the warranty claims. The noisy brakes give an impression of faulty brakes which is perceived as a loss of quality and hence a negative brand image among the customers.

The overall aim of this thesis was to investigate the source of brake noise, which was found in a previous study [1] to be the interface between the brake pad and rotor, and gain insight into the vibration characteristics of the disc brake system. The following research question was proposed for the thesis: ***Can the bicycle brake noise at the pad-rotor interface be predicted via Finite Element Analysis and can a countermeasure to reduce the brake noise be devised?***

The objectives of the current research are:

- To perform experimental modal analysis using the optical interferometry technique to establish the vibration characteristics of the brake assembly during the brake noise events
- To model the brake components (rotor, brake pads, and caliper) of the bike used in experiments on Solidworks 2020 SP4 and develop a simple yet detailed finite element model for the analysis on ANSYS Workbench 2021-R2
- To execute a modal analysis at the component level and correlate with the brake components
- To conduct a comprehensive finite element prestressed modal analysis using a complex eigenvalue method to establish the natural frequencies and the mode shapes of the brake assembly and compare it with the experimental interferometric data
- To determine how many decibels do the countermeasures lower the brake noise by

This report consists of eight chapters. Chapter 2 covers a number of background theories and frictional models explaining the friction-induced instabilities. Chapter 3 presents the experimental investigation method and the test bench that was used to perform the experimental modal analysis. Chapter 4 concentrates on the experimental results and presents the key observations from the experiments. Chapter 5 introduces the numerical simulation methods and the procedure of the finite element process that was adopted to design and simulate sliding contact in ANSYS. Chapter 6 presents the finite element analysis results and focuses on the comparison with the experimental studies performed in chapter 4. Chapter 7 covers the countermeasures, both the experimental and computer simulations of some of the ways to reduce the brake noise levels. Finally, chapter 8 concludes the study and provides the outcomes of the study and future recommendations.

2
Background

In terms of their structure and interaction with the surrounding elements, the sounds that the bicycle brakes produce have opposite qualities to those of the violin. Within brakes the noises are produced through various instability mechanisms, where the response of the system is often the mode lock-in, which happens between more than one fundamental frequency.

The frictional brakes convert most of the kinetic energy of the bike into thermal energy within the rotor and the pads but some of the kinetic energy is converted into the vibrations that travel throughout the structure of the bike. These vibrations often result in the sound radiations that can involve a number of components of the brake system.

The brakes that are noisy do not produce noise during every braking action. Brake noise is a rather random event and many factors contribute to the brake noise generation. A number of theories that explain the random brake noise mechanism have been formulated and a few of them are discussed in this chapter.

2.1. Stick-slip

The stick-slip behavior can be modeled as a spring-mass system as shown in Figure 2.1. While decelerating, the friction force at the interface increases until the relative motion stops. When this friction force exceeds the static threshold, the stored potential energy in the system is released and acceleration occurs, which results in a lower dynamic friction coefficient. As the slipping mass catches up with the oscillator and starts to decelerate, the friction force rises again and the entire process repeats. During the slipping phase, there is a temporary loss of surface contact between the mass and the oscillator surface, therefore the stick-slip behavior is not reflective of changes in μ as a function of time but only changes in tangential force as a function of time.

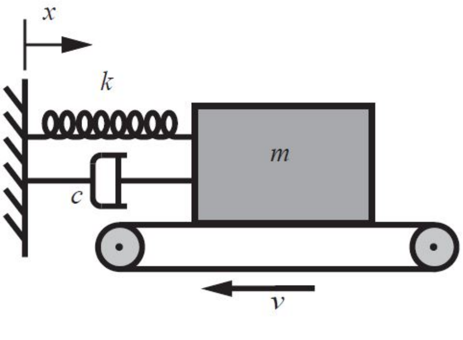

Figure 2.1: Spring-mass-damper system sticking and slipping on the moving surface

In 1938, while examining the drum brakes, Mills [15] discovered a trend of decreasing dynamic

friction coefficient, μ_k with increasing rotor speed, v_s. This discovery led to a school of thought which advocated, that for brake noise to occur, the presence of a $\mu_k(v_s)$ relationship was necessary.
The governing equation of the oscillator is [13]

$$m\ddot{x} + (c - mg\mu)\dot{x} + kx = 0$$

where m is the mass, k is the stiffness, c is the damping, μ is the friction coefficient, and x is the displacement of the mass from the equilibrium. When $\mu > c/mg$, it introduces a negative damping and the self excited vibrations in the system. Therefore, disc brake noise has the characteristic of frictional vibrations induced by the friction pair having a dynamic friction coefficient which decreases with the increase in speed. This decreasing friction coefficient value with increasing sliding velocity introduces the random friction induced instabilities in the system that often result in acoustic energy [13]. Mills concluded in his work that the stick-slip action at the interface of the brake pad and the drum produces a squeak, which is similar in a way to the violin string and its bow, where the source of energy is the variation in the friction force with speed.

2.2. Sprag-slip

Sprag-slip is another unique instability phenomenon in contact sliding systems. Sprag-slip theory, established by Spurr, says that the friction force can increase significantly above its normal level because of the geometric constraints of the interface and then at some level come back to its normal state because of the plastic/elastic deformation of the contact surface. Its occurrence depends on the structural configuration and the interface constraints that bring in the changes in the normal and frictional forces. According to Spurr, a locking action of the slider on the sliding surface causes a sprag-slip. The locking happens when one of the sliding components is hinged at an acute angle to the sliding surface. Consider the system in Figure 2.2, where a beam is hinged at point O and contacts the sliding surface at an acute angle. From Coulomb's law, we know that $F_f = \mu F_N$. At equilibrium the equations are:

$$F_N = \frac{L}{1 - \mu tan\theta}$$

$$F_f = \frac{\mu L}{1 - \mu tan\theta}$$

When μ approaches $cot\theta$, F_f approaches infinity. This critical case is called spragging. When this beam is considered rigid, the motion halts during spragging. However, in reality, that is not the case and there is an element of elasticity and plasticity in the beam, which allows it to release by slipping from the spragging situation due to its flexibility. The flexible beam deforms under the large normal and frictional forces to relieve sprag. This sprag-slip situation keeps rebuilding and just like stick-slip, the cycle continues.

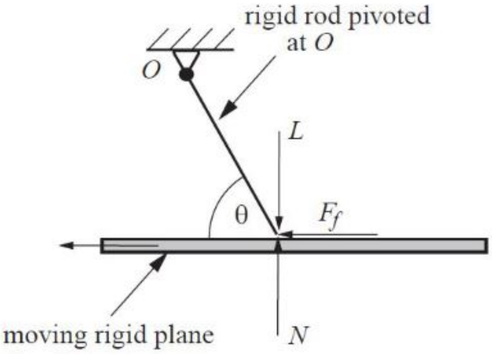

Figure 2.2: A rigid, massless beam, which is pivoted at O and loaded with an external force L showing geometric coupling

At the time of sprag, the salient asperity of the sliding surface slide towards the hinged arm, the friction force increases the normal load that ultimately causes the halt. The flexibility in the arm allows the asperity to creep and pass the arm. This motion of the salient asperity away from the arm decreases the normal force. That is why sprag-slip is known as geometrically induced or kinematic constraint instability that can occur even at the constant coefficient of friction.

2.3. Mode lock-in

The mode of a vibrating circular disc is the frequency at which the different sections of the disc vibrates. This frequency can be determined by counting the number of nodal circles and nodal diameters. Node define the points on the vibrating body where the disc medium remains at rest. Therefore, the nodal diameters and nodal circles are the lines and the circles on the disc where the medium does not move. Unlike uni-dimensional vibrating strings, vibrating circular discs have vibrations in the 3-D space. Vibrations of the disc in the XY plane (see Figure 2.3) are called in-plane vibrations and the modes associated with those are known as in-plane vibration modes. Out-of-plane vibration modes of the disc lie in the YZ plane. For a circular disc or a membrane, the nomenclature to label modes is (d,c) where d is the number of nodal diameters and c is the number of nodal circles on the vibrating circular body. Figure 2.4 displays the nodal patterns of a circular disc with their respective mode shape nomenclature [19]. This nomenclature is used to describe out-of-plane modes of the vibrating circular disc. The modes that only have nodal diameters are known as diametric modes and the modes that only have nodal circles are known as concentric modes. Out-of-plane modes are the combinations of the diametric and concentric modes.

In a disc brake system, each brake component has its own dynamic characteristics. If two brake components have close range natural frequencies, their dynamic motions lock-in geometrically, which establishes an energy flow between them and leads to an increase in the vibration amplitudes. This process by which modes of two different sub-structures couple together resulting in a resonant response is known as ”mode lock-in” [5]. Akay [4] pointed out distinct types of mode lock-in that can be present in a system. The **classical mode lock-in** is the type in which modes of the components are almost equal in frequency and thus a lock-in occurs at that frequency. Another type of lock-in is the **intermediate mode lock-in** where the system locks onto a frequency that lies in between the eigen frequencies of the components. The last type of lock-in is called **multiple mode lock-in**. This is the type where the doublet modes along with the other types of lock-in occur in a system simultaneously. In the multiple lock-in, the squeal spectrum not only consists of one dominant frequency and its harmonics but also the sidebands.

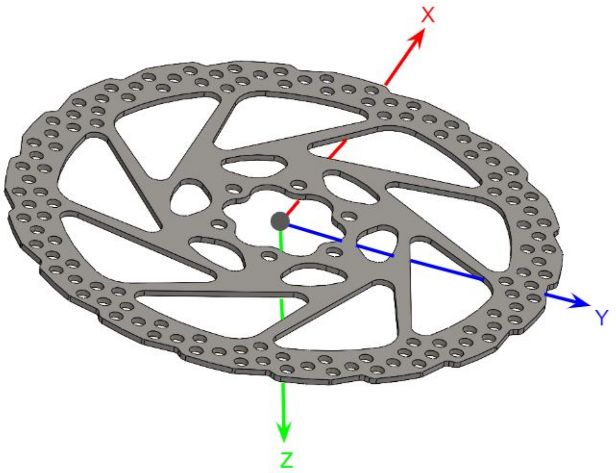

Figure 2.3: The circular disc vibrates in a 3-D space; the vibrations of the disc in the XY plane are known as in-plane vibrations and the vibrations in YZ plane are known as out-of-plane vibrations

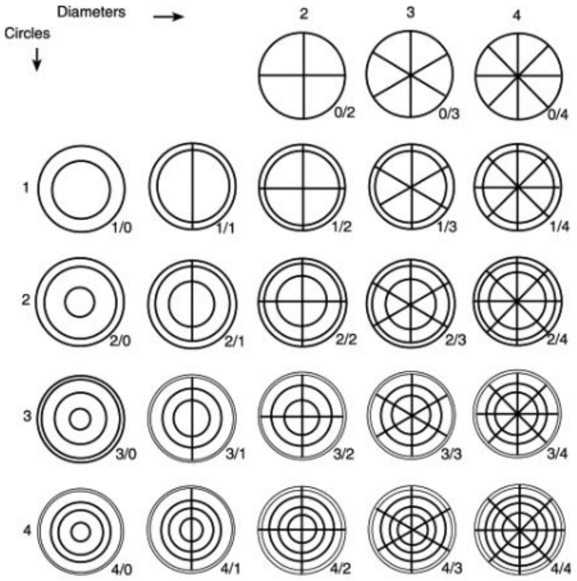

Figure 2.4: Mode shapes of a circular disc with their respective nodal circles and nodal diameters [19]

2.4. Doublet modes

A doublet mode describes two modes with the same diametric and concentric modes that lie within close range frequencies to each other but with a different phase. Splitting of doublet modes or flutter instability theory was first presented by Mottershead and Chan [9]. They noted that in a symmetric rotor, the frequency of eigen modes split into the doublet modes. This splitting of modes led to flutter which was equated to squeal. They concluded their study by suggesting that the frictional mechanism that had been the subject of the research for past 4-5 decades is now of secondary importance and flutter instability as a sole cause of brake noise be studied further. Lang et al [14] and Nishiwaki et al [17] in their separate studies of brake squeal observed the doublet modes. They performed studies to investigate these modes and concluded that the doublet modes often converge together during vibration and induce system instabilities.

In summary: The symmetrical structures have a tendency where their eigen modes split into two modes with the same mode shape and then converge together causing a flutter instability in the system.

2.5. Stick-slip and Modal coupling

Rhee et al. [20] argued that frictional mechanisms and mode lock-in together causes instabilities in the brake system. They were of the view that the friction-induced instabilities caused by the stick-slip, where the waves of detachment can be viewed as series of impulses acting at the frictional interface. These impulses act like a hammer and excite the natural frequencies of the brake system components. After an initial excitement due to the frictional instabilities the modal coupling causes a resonance between the components, which increases the amplitudes of vibration in the structure ten folds.

2.6. Energy Balance

One of the by-products of friction is heat generation. The temperature has a tremendous influence on the brake performance. The temperature of a sliding contact affects the friction coefficient, which tends to rise with the increase in temperature. According to thermodynamics, at equilibrium, the amount of energy into the system U_{in} equals the sum of energy leaving the system U_{out} and the energy stored/consumed by the system $U_{accumulated}$.

$$U_{in} = U_{out} + U_{accumulated}$$

The energy input at the interface due to friction is balanced out by heat conduction, vibrations, and sound. When there is more energy input into the system than the system can dissipate, it leads to most of the friction-excited vibrational instabilities and also the sound radiations [4]. At the micro/nano level, which corresponds to the interatomic distances, friction acts as a dissipation mechanism, converting kinetic energy into different forms of energy. This level also forms the upper limit of acoustics. This means the aspect of friction where energy transformation takes place is an acoustical process. By better heat conduction, most of the energy that is dissipated is transformed into heat and into less vibrations and sound radiations.

3

Experimental Investigation into Brake Noise

This chapter gives an outline of the experimental methods that were followed in the study. It provides information about the bicycle components and the test bench that were used for data collection. The design of experiments for the purpose of this study and the reasons for the choice of experimental runs are also described in this chapter. Lastly, the limitations of the experimental setup are also discussed.

3.1. Description of the test bench

This section is subdivided into three subsections. First subsection presents the characteristics of the brake test machine that is used to run the bicycle in the laboratory settings. Second subsection presents the bicycle components that are used during data acquisition and the third subsection describes the data acquisition equipment.

3.1.1. Brake test machine

A dedicated brake test machine (see Figure 3.1) designed and manufactured by Schmidt-Engineering GmbH was used to investigate disc brakes for this study. The test machine was developed according to the bicycle test standards: **ISO 4210-4**, **DIN EN 14764**, and **EN15194**. This brake test machine is designed to work best in 20 - 25^0C and 45-50 humidity. One of the unique features of the brake test machine is that it is designed to test the bike in its fully assembled state. This means the brake system need not be isolated and the dynamics and interactions of the components surrounding the brake assembly are captured during testing.

The rear wheel of the bicycle is fixed and the front wheel is installed on the roller that runs the wheel. The front wheel is kept in place using movable fixtures that maintain the wheel at the center. These fixtures also apply downward pressure to simulate the weight of a 100 kg person on the front wheel. The braking action is performed by the lever actuator cylinders fixed on the handlebar. The inputs to the brake test machine are given via the DASYLab software, which controls the braking force on the handlebar, roller drum speed, and the pressure on the front wheel. The outputs of the brake test machine are the braking force at the caliper and the outputs of the bicycle on the brake test machine are the vibrations of the bicycle components and the brake noise. Another feature of the test bench is the ability to test brakes in wet and dry conditions. The nozzles as shown in Figure 3.2 spray water onto the rotor pad interface simulating the wet weather conditions.

3.1.2. Bicycle components

Gazelle Medeo T10 HMB known for its high squeal propensity was selected as the bicycle for this particular investigation. The bicycle was equipped with a Suntour NEX E25 HLO front fork. Shimano disc brake components were used for this present study.

Shimano BR MT200 caliper and sport type resin Shimano brake pads were used for the experiments as shown in Figure 3.3. The caliper is a 2 piston fixed type caliper with one piston on each side. It

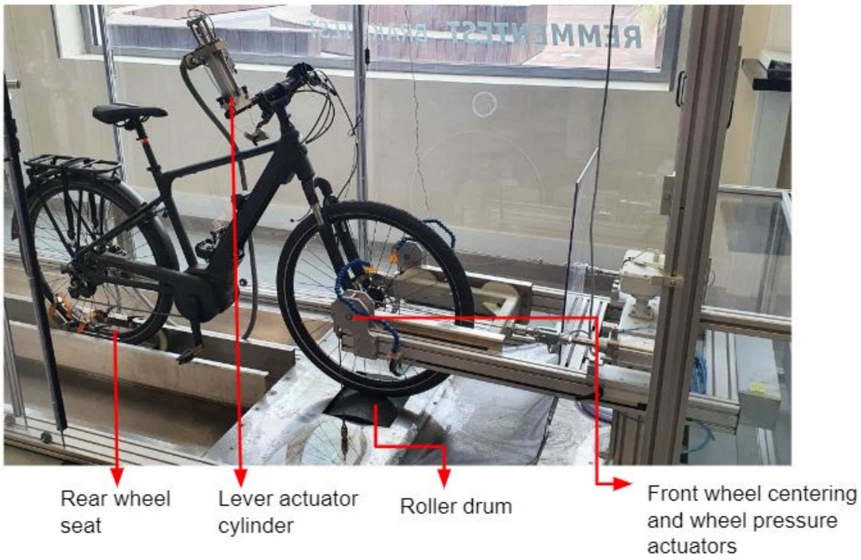

Figure 3.1: A dynamic brake test machine used for experimental investigation designed by Schmidt-Engineering GmbH to test bicycle brakes

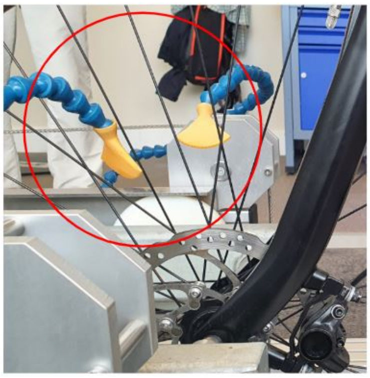

Figure 3.2: Yellow nozzles in the red circle used to spray water onto the rotor and pad interface

is specifically designed for the e-bikes and allow a uniform pressure distribution on both sides of the caliper for better control of the clamping force on the rotor. According to the brake manufacturers' website, the sports resin pads are known to be quieter than the other brake pads on the market. Shimano Deore RT56 rotor was used in the experiments. The rotor is 180 mm wide and 1.8 mm thick. The part list is summarized in the Table 3.1

Bicycle Parts	Model
Bicycle	Gazelle Medeo T10 HMB
Front fork	Suntour NEX E25 HLO
Caliper	Shimano BR MT200
Brake pads	Sport type resin
Rotor	Shimano Deore RT56

Table 3.1: Summary of the bicycle disc brake components and the surrounding parts used in the experimental runs

3.1.3. Data acquisition

The two outputs of the bicycle on the brake test machine i.e. the vibrations of the bicycle components and the brake noise are captured for further data analysis. Brake noise audio measurements and the interferometric measurements are performed to collect the outputs.

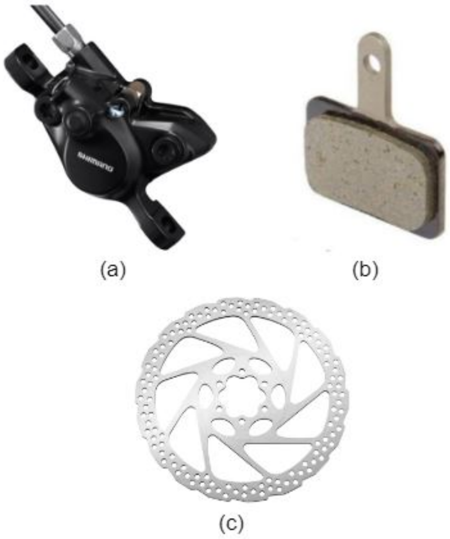

Figure 3.3: Brake components used in the experimental investigations (a) Shimano BRMT200 caliper (b) Shimano B01S resin brake pads, (c) Shimano Deore RT56 rotor

Brake noise audio measurements

Brake noise audio data is captured using a BOYA BY-M1 microphone mounted close to the sliding surface of the rotor and pad as shown in Figure 3.4. The brake noise data is captured to identify the brake noise frequencies by plotting the Amplitude Vs. Frequency graphs. A simple MATLAB code is written to extract the frequencies and the magnitude from the audio recordings (Appendix A).

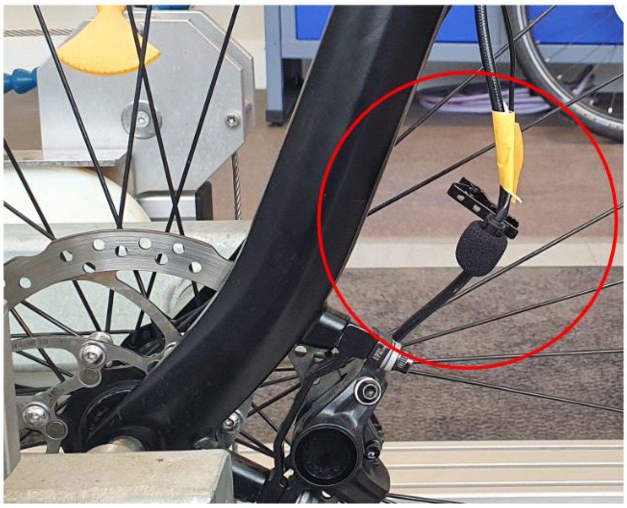

Figure 3.4: Microphone placement near to the frictional interface to capture the brake noise audio data

Interferometric measurements

In addition to the brake noise audio scans, the optical interferometry technique is used to capture the out-of-plane vibration velocities of the rotor, caliper, and the front fork. These measurements are done to identify the source of vibrations and investigate the vibration propagation from the source to the surrounding components. Optical interferometry was first utilized by Newcomb and Fieldhouse [10], where they were able to generate mode shapes of the vibrating bodies. Similarly, for this study, interferometric measurements are used to perform experimental modal analysis and generate mode shapes of the brake assembly and the front fork. The important point to note here is that the mode shapes that are generated, capture the vibration characteristics of the brake components while they are interacting with each other. Another unique feature of optical interferometry is that it allows for non-contact vibration measurements and captures vibration amplitudes of rotating bodies like rotors, which are hard to get with accelerometers.

The setup for the optical interferometry consists of a PSV-400 laser vibrometer head and the QTec reference head. While the laser vibrometer head focuses the laser on the vibrating components, the reference head focuses a laser beam on the surface that is not vibrating to form a reference for the vibrometer head.

The laser Doppler vibrometer was able to capture the vibration velocities of the brake caliper and the front fork but not of the rotor when the bicycle is run on the brake test machine. The vibrometer head needs a clear and unrestricted view of the brake components to capture their vibration amplitudes accurately. Because the brake test machine covered most of the rotor surface and blocked the view of the vibrometer to capture the rotor vibrations, a treadmill was used to run the bicycle to allow for accurate interferometric measurements of the rotor. The setup of the laser Doppler vibrometer head and the reference head with the bicycle on the treadmill is shown in Figure 3.5.

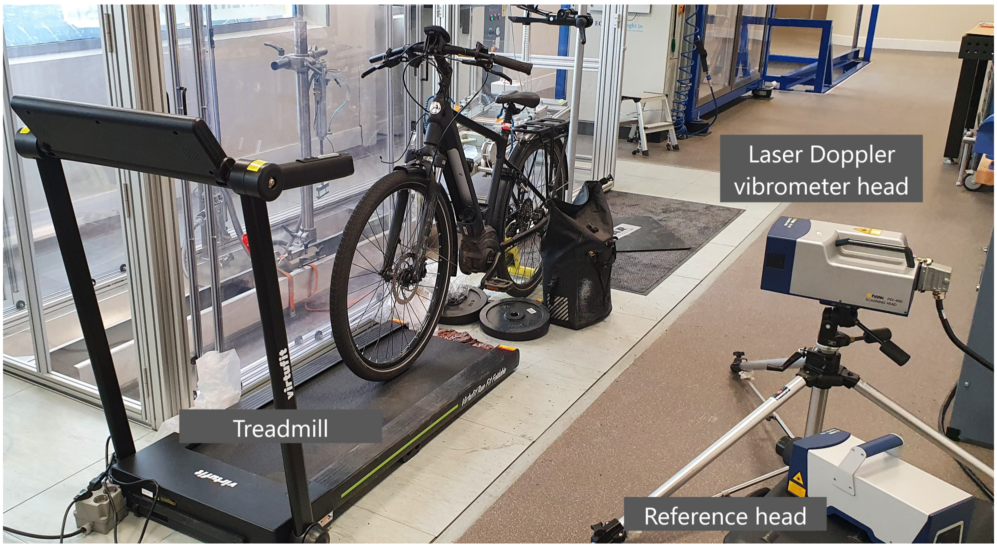

Figure 3.5: Test bench with treadmill to run the bike with an unrestricted view of the rotor for the laser vibrometer to capture the vibration velocity

The laser vibrometer is placed such that the laser beam is perpendicular to the vibrating surface. The laser beam is then focused at the point of interest by clicking on the focus icon on the Polytec software. The signal strength at the point of interest is checked in the software and maintained above the threshold limit of 20 percent as suggested in the manual for accurate results. The signal strength can be increased by using aluminium tape, which increases the reflectivity of the surface to be measured. In the next step, the measurements per point are set to three. The software calculates the average of the three measurements. Three measurements per point provided a good balance between the time taken to perform the experimental run and the accuracy of the data collected. The bandwidth of 200-5000 Hz was chosen to identify the vibration frequencies of the brake components. A 2D alignment between the mouse pointer on the screen and the laser beam pointer on the bicycle component was performed on the software. This aligns the laser pointer with the software and the beam position can then be controlled and stored in the software. The grids as shown in Figure 3.6 are created on the brake components manually by plotting the grid points on the areas of interest. The software then commands the laser vibrometer to drop the laser beam at every point on the grid and measure the out-of-plane vibration amplitude at those points. The vibration modes and the magnitude Vs. frequency plots are derived from the software. The vibrometer head used in the experiments could only measure the out-of-plane mode shapes and no in-plane mode shapes were captured.

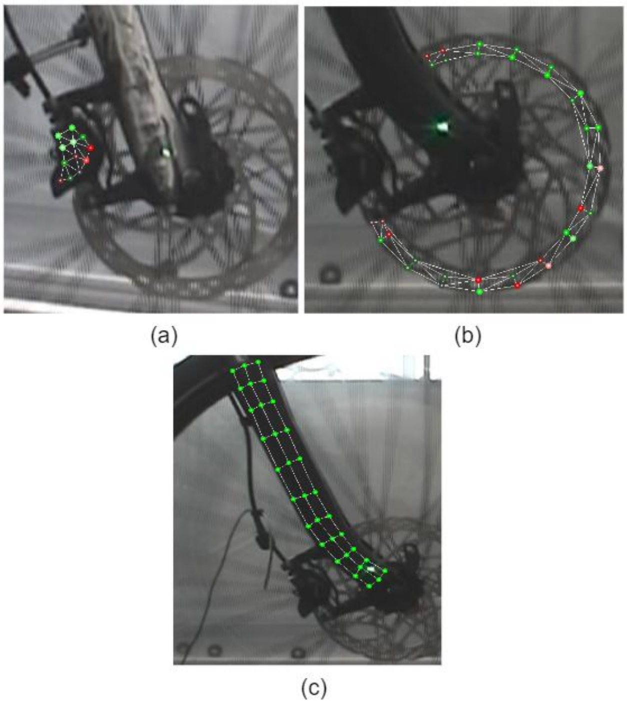
(a) (b)

(c)

Figure 3.6: Creation of mesh on the vibrating brake components for the laser beam to follow and collect the vibration data at all the points of the mesh (a) Mesh on the rotor (b) Mesh on the caliper (c) Mesh on the front fork

Limitations

The Polytec PSV-400 laser vibrometer head that is used in the present study can only measure the out-of-plane vibrations of the bicycle components. In Figure 3.7 the YZ plane is referred as the out-of-plane vibration plane and the XY plane is referred to as the in-plane vibration plane for this project. The Polytec IPV-100 laser vibrometer head that can measure the in-plane vibrations could not be used because of the financial constraints. Therefore, the information regarding the vibration characteristics of the bicycle components in the in-plane direction is not studied experimentally. Experimental study by Nakae et al [16] was referred to fill in the missing pieces of the in-plane vibration modes.

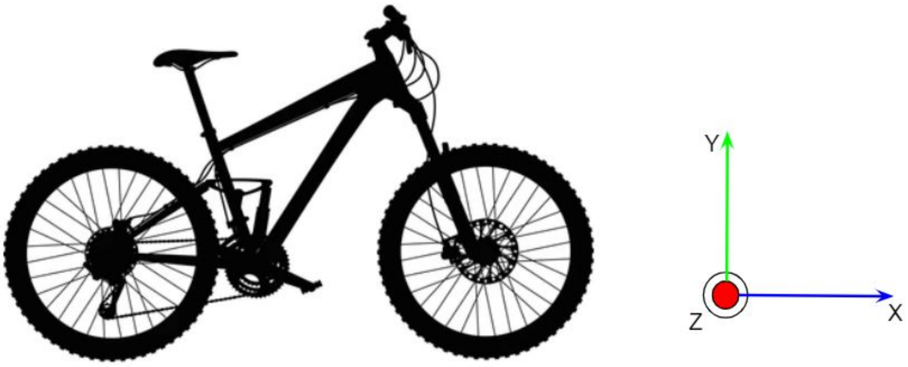

Figure 3.7: The XY plane vibration modes of the bicycle components are referred to as the in-plane vibration modes and the YZ plane vibration modes are referred to as out-of-plane vibration modes for this project

3.2. Test procedure

Bed-in process and the process to warm up the pads and the rotor referred to as ”Warm-up process” in this report are discussed in this section. These processes are carried out to ensure that all the test runs are initiated with similar conditions. Figure 3.8 gives an overview of the test procedure that was followed.

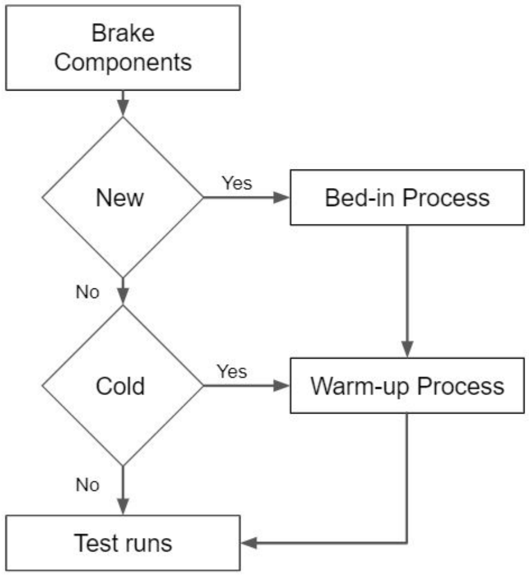

Figure 3.8: Flow chart depicting how the experiments were conducted; the ”Bed-in process” was followed for all the new brake pads and the rotor and the ”Warm-up process” was followed so that tests were not run with cold brake parts

3.2.1. Bed-in process

It is highly recommended that all the new rotors and the brake pads are properly bed-in before they are used in order to extract the best performance from the brakes and for quieter braking. The bed-in process heats up the pads and the rotors, depositing an even layer of the frictional material onto the sliding surface of the rotor. This transfer layer is very important to optimize the braking in the bicycle.

The bed-in process was conducted by manually riding the bike. The bike was brought to a moderate speed of 10 km/hr and then brakes were evenly applied to bring the bike speed down to 4 km/hr. This acceleration and deceleration completed one run, and 20 such runs were conducted. After the initial 20 runs, the bedding-in process was ended with 10 runs by running the bike at a faster speed of 14 km/hr and then decelerating it to 4 km/hr. These 30 runs completed the bed-in process of one rotor and brake pad pair.

3.2.2. Warm-up process

Before every run, it was made sure that the brake system: pads, and rotor were not run cold. This step was important because of the uncertainty in brake noise generation during the experimental runs. Therefore, to kick the uncertainty factor out and to induce the brake noise as best as possible the warm-up process was carried out before every run.

The bike was run at 12.5 km/hr with a force of 40 N applied at the handlebar for 3 seconds and then a 3-second cool-down, which completed one run. Ten such runs were completed before the data from the brake test machine was captured.

This process heated up the pad and rotor interface enough to induce brake noise and remove any uncertainties in the data collection. After the kick-off process, the bike was run at 5 km/hr and braking action was performed by applying 80 N force on the handlebar for data collection.

Test Run	Interferometric Measurements	Audio Measurements	Running Conditions	Weather Conditions
1	Rotor	Yes	5 km/hr, 80 N Brake noise events	Wet
2	Rotor			
3	Front Fork			
4	Front Fork			
5	Caliper			
6	Rotor			Dry
7	Rotor			
8	Front Fork			
9	Front Fork			
10	Caliper			
11	Rotor	NO	5 km/hr, 80 N No noise events	
12	Rotor			
13	Front Fork			
14	Front Fork			
15	Caliper			

Table 3.2: Summary of the test runs where interferometric measurements column indicate the bicycle part that is scanned via the vibrometer and the audio measurements column indicate if the brake noise audio was recorded

3.2.3. Test runs

The audio measurements and the interferometric measurements were performed simultaneously. For the measurements the bicycle was run at a constant speed of 5 km/hr. A braking force of 80 N on the handlebar, which translated to 263 N at the caliper, was applied. The bicycle was tested under wet and dry conditions both. The brakes under wet conditions always produced noise. During dry runs the brakes did not always produce noise and there were certain runs where no brake noise was captured. The runs where no brake noise was heard are termed as no noise events and the runs where brake noise was heard are termed as brake noise events.

A total of five test runs under wet conditions were performed. During each run interferometric measurements of one bicycle component and the brake noise audio measurements were conducted. Because of the large number of measurement points of the mesh of the rotor and the front fork, they were scanned twice to remove any uncertainty in the collected data and to check the reproducibility of the measurements. Similarly, a total of five test runs under dry conditions were also conducted. Table 3.2 presents a summary of the test runs where interferometric measurements column indicate the bicycle part that is scanned via the vibrometer and the audio measurements column indicate if the brake noise audio was recorded

4

Experimental Results

In this chapter the results of the test runs performed in chapter 3 are presented and discussed. The brake noise audio data collected during the test runs was further analyzed in MATLAB R2020b to generate the Amplitude Vs. Frequency plots. The frequency plots were used to understand the acoustic behaviour of the brake noise. The decibel levels of the brake noise was measured via the sound meter app for Android.

The interferometric measurements of the bicycle components revealed their dynamic characteristics (i.e. natural frequencies and the mode shapes) during the brake noise and no noise events. The vibration Magnitude Vs. Frequency plots of the caliper, rotor, and the front fork were generated via the Polytec software for both the brake noise and no noise events. The interferometric data sheds more light on the vibration behaviour of the bicycle components under brake noise and no noise events.

4.1. Audio Scan results

There were three peak frequencies found in the audio scans of the brake noise. The first peak was found in the frequency range of 550-650 Hz, the second peak was in the region of 1100-1250 Hz, and the third peak lied in the range of 1750-1850 Hz. In this report, the first frequency peak range is called the chatter region, the second frequency peak region is called the squeal region, and the third frequency peak region is called the high-frequency squeal region.

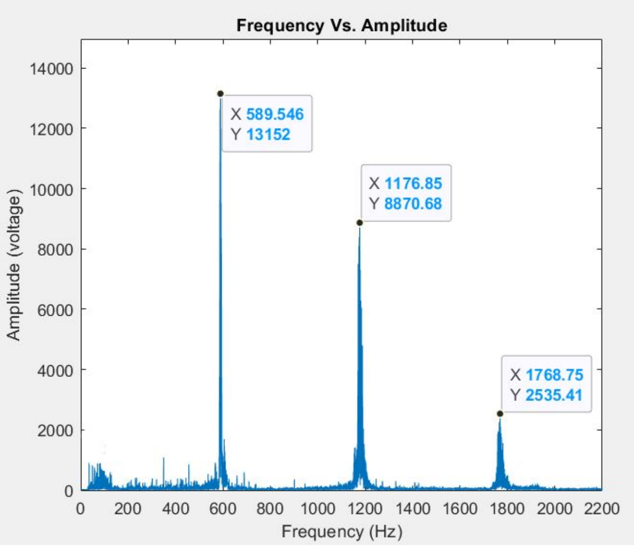

Figure 4.1: Amplitude Vs. Frequency plot of the test run 8 revealing three peak frequencies; first peak is the chatter range, second peak is in the squeal range, and the third peak is in the high-frequency squeal range

Test Run	Frequency (Hz)			Amplitude (voltage)		
	Chatter	Squeal	High freq. Squeal	Chatter	Squeal	High freq. Squeal
1	586.3	1175.0	1758.3	4135.7	5752.3	610.8
2	587.9	1180.5	1769.0	3929.6	5362.2	566.7
3	587.2	1179.3	1766.6	3429.1	4980.4	487.2
4	588.5	1180.9	1770.8	3620.2	5306.3	447.6
5	587.9	1182.3	1770.2	2122.3	4525.9	446.1
6	588.1	1176.8	1768.7	11378.5	7605.8	3684.7
7	590.9	1181.9	1771.5	12925	5904.4	2706.1
8	589.5	1176.8	1768.7	13152	8870.6	2535.4
9	591.6	1189.9	1772.4	15941	7604.1	2353.3
10	592.6	1175.2	1774.2	13566	6866.6	1097.6

Table 4.1: Summary of the Audio measurements of the test runs with the frequency peaks in the chatter, squeal, and high frequency squeal regions; the blue rows are wet runs and the yellow rows are the dry runs

Figure 4.1 shows the Amplitude Vs Frequency plot of the Test run 8 with three peak frequencies. The three peaks maintained almost similar frequencies during all the test runs as seen in the Table 4.1. The Amplitude Vs. Frequency plots of all the test runs are presented in Appendix B. The squeal to chatter ratio was 2 and the high-frequency squeal to squeal frequency ratio was always 1.5. With a change in weather conditions, the frequency of the brake noise did not vary but the magnitude was affected and the difference can be seen in blue and yellow rows of the Table 4.1. During the dry weather conditions (seen in yellow), the chatter noise magnitude was greater than the squealing noise. The squealing noise, however, dominated the chatter noise under wet weather conditions(seen in blue).

The brake noise was measured at 97±5 decibels. To put it in perspective, the lawn mower also records 95 decibels, so the brake noise of a bicycle is comparable to the noise from a lawn mower. NIOSH (National Institute of Occupational Safety and Health) recommends the noise exposure limits of 85 decibels and the bicycle brake noise exceeds it by a lot.

4.2. Vibrometer Results

While audio scans only provided information about braking events when there was brake noise, the vibrometer data presented information for both the noise and no noise events.

Figure 4.2 shows the vibration velocity Magnitude Vs. Frequency plots of the caliper, rotor, and the front fork under brake noise events. These plots are highly correlated with the audio scan plots. Table 4.2 summarises the vibration frequency and the magnitude of the bicycle parts for all the test runs scanned via laser vibrometer; the blue rows are for the wet weather conditions and the yellow rows are for the dry weather conditions. The maximum rotor vibration velocity was observed at 1.61 mm/s during Test run 1, the maximum caliper vibration velocity was observed at 1.17 mm/s during Test run 5, and the maximum front fork vibration velocity of 427 μm/s was observed during the Test run 4. All the maximum vibrations of the bicycle components were found in the chatter region as revealed by the Table 4.2.

Not all braking events were noisy and Figure 4.3 shows the frequency plots of the brake components under the no brake noise condition. It can be seen from the Table 4.3 that the brake system vibrates completely differently in the no brake noise events. There lies no peaks in chatter„ squeal and high frequency squeal regions and the magnitude of vibrations is also very less. Under no noise events the rotor vibrated the maximum out of all the brake components at a vibration velocity of around 250 μm/s. The caliper and front fork both vibrated at a velocity of around 30 μm/s. There were no unique peak frequencies for no noise events.

Figure 4.4 displays the mode shapes of the rotor under the brake noise conditions as derived via optical interferometry. The mode shape for the rotor in chatter was (2,1), in squeal it was (3,1), and in high-frequency squeal it was (4,1). The gray areas indicate the nodes and the red and green regions

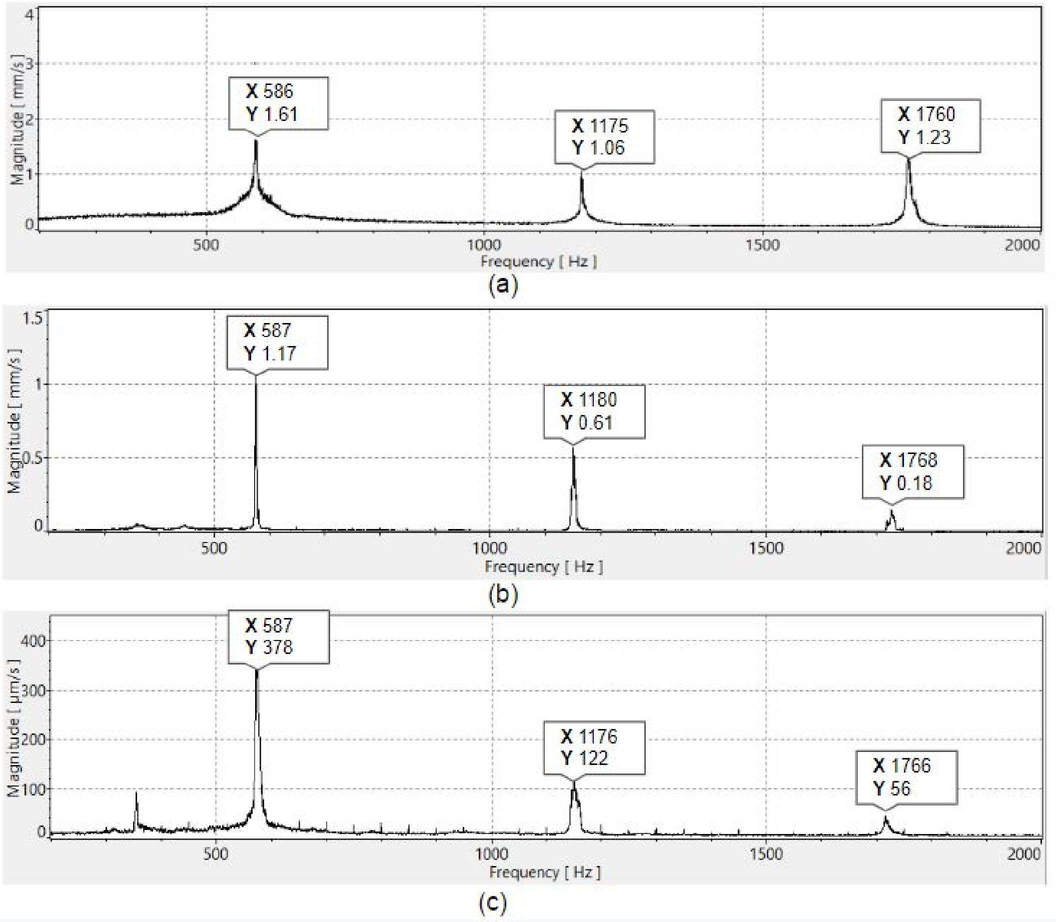

(a)

(b)

(c)

Figure 4.2: Magnitude Vs. Frequency plots of vibrating bicycle parts under brake noise events as generated by the Polytec software for (a) Rotor (b) Caliper (c) Front fork

Test Run	Part scanned	Frequency (Hz)			Magnitude		
		Chatter	Squeal	High freq. Squeal	Chatter	Squeal	High freq. Squeal
1	Rotor	586	1175	1760	1.61 mm/s	1.06 mm/s	1.23 mm/s
2	Rotor	587	1177	1769	1.58 mm/s	1.26 mm/s	0.44 mm/s
3	Front Fork	587	1176	1766	378 μm/s	122 μm/s	56 μm/s
4	Front Fork	589	1180	1768	427 μm/s	242 μm/s	31 μm/s
5	Caliper	587	1181	1771	1.17 mm/s	0.61 mm/s	0.18 mm/s
6	Rotor	588	1178	1769	674 μm/s	296 μm/s	32 μm/s
7	Rotor	590	1182	1774	569 μm/s	352 μm/s	36 μm/s
8	Front Fork	589	1177	-	294 μm/s	49 μm/s	-
9	Front Fork	590	1189	-	401 μm/s	82 μm/s	-
10	Caliper	588	1176	1770	552 μm/s	372 μm/s	113 μm/s

Table 4.2: Summary of the vibrometer scans of the test runs with the frequency peaks in the chatter, squeal, and high frequency squeal regions; the blue rows are wet runs and the yellow rows are the dry runs

indicate the positive and negative displacement of the rotor.

The vibration mode shapes of the front fork under brake noise events are shown in Figure 4.5 for the chatter and squeal regions only. The high-frequency modes are not studied for the fork because of their insignificant vibration velocity in the higher frequency regions.

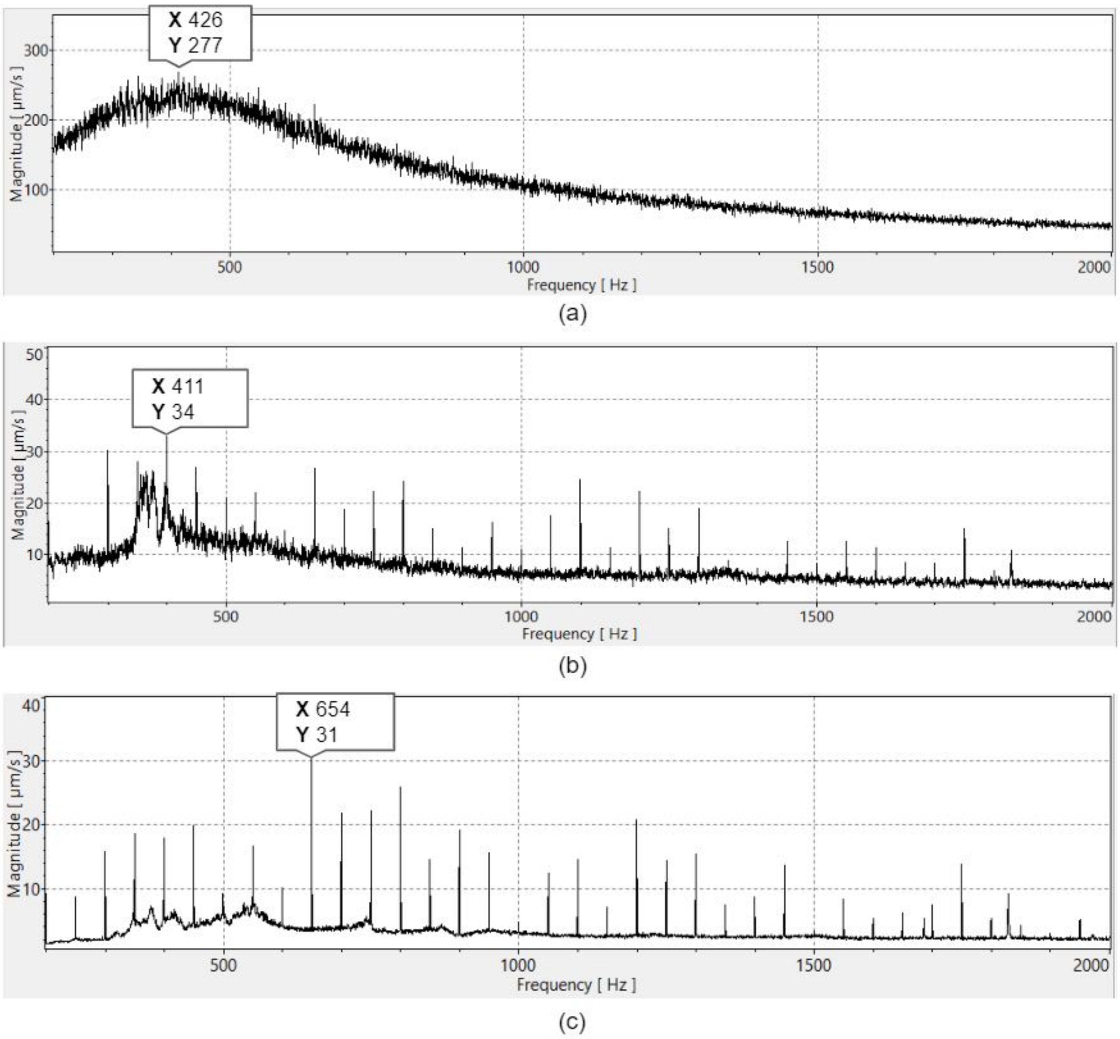

Figure 4.3: Amplitude Vs. Frequency plots of vibrating bicycle parts under no brake noise events (highlighting the maximum magnitudes) for (a) Rotor (b) Caliper (c) Front fork

Test Run	Part scanned	Maximum Frequency (Hz)	Maximum Magnitude (μm/s)
11	Rotor	426	277
12	Rotor	432	271
13	Front Fork	654	31
14	Front Fork	660	26
15	Caliper	411	34

Table 4.3: Summary of the vibrometer scans of the no noise test runs with no peaks observed in the chatter, squeal, and high frequency squeal regions

4.3. Investigation into the randomness of brake noise

To investigate why certain braking events were noisier and certain braking events quieter, the dynamic friction coefficient of the frictional surface was calculated on the brake test machine. The random nature of brake noise strongly suggested a presence of friction-induced instability in the system. The Brake test machine outputs were brake distance 's' and brake force 'N' at the rotor pad interface. The knowns were initial velocity 'u', final velocity 'v', and the mass 'm' of the rider and the bicycle. The unknowns

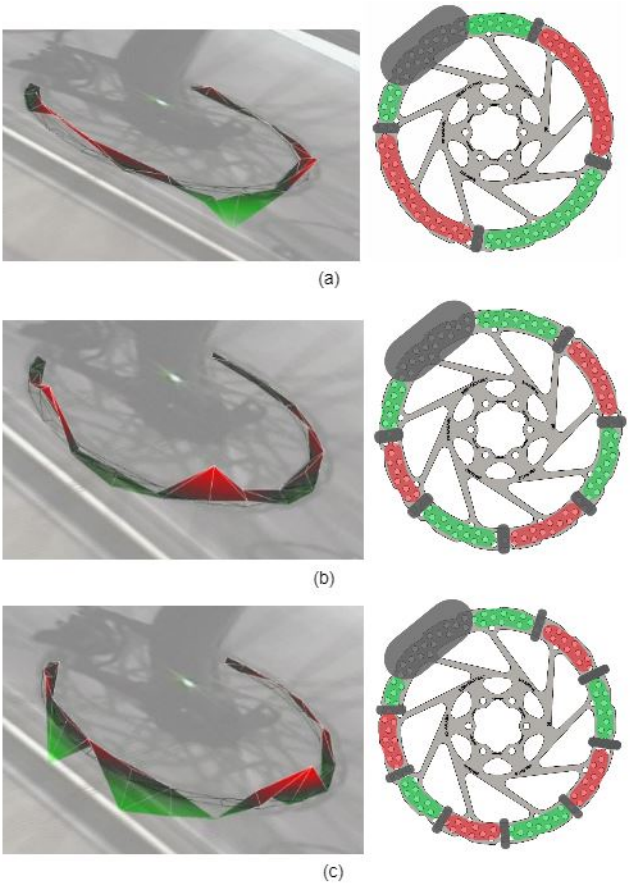

Figure 4.4: Mode shapes of the rotor scanned by laser Doppler vibrometer during brake noise event; gray areas indicate the nodes and the red and green regions indicate the positive and negative displacement of the rotor. On the left are the mode shapes captured by the vibrometer and on the right are the schematic sketches of the mode shapes (a) Chatter: 587 Hz, (b) Squeal: 1177 Hz, (c) High-frequency Squeal: 1769 Hz

were friction force 'F'. The coefficient of friction 'μ' is

$$\mu = \frac{F}{N} \tag{4.1}$$

from Newton's law

$$F = ma \tag{4.2}$$

using third equation of motion

$$v^2 - u^2 = 2as \tag{4.3}$$

$$a = \frac{v^2 - u^2}{2s} \tag{4.4}$$

Substituting (4.4) and (4.2) in (4.1) gives us the value of friction coefficient. Figure 4.6 shows a trend of decreasing friction coefficient with the increase in cycling speed that indicates the presence of stick-slip in the system.

4.4. Discussion

The brake noise audio scans reveal that during a brake noise event we hear three peak frequencies, i.e. chatter, squeal, and high frequency squeal. The absolute frequencies of the three peaks for all the test runs remained fairly consistent around 588 Hz, 1176 Hz, and 1764 Hz. It was found out from the audio scans that the chatter magnitude under dry conditions was significantly higher than under the wet weather conditions. One possible cause of this magnitude change in chatter can be attributed to the temperature change that might happen at the sliding interface of the rotor and the pads due to the

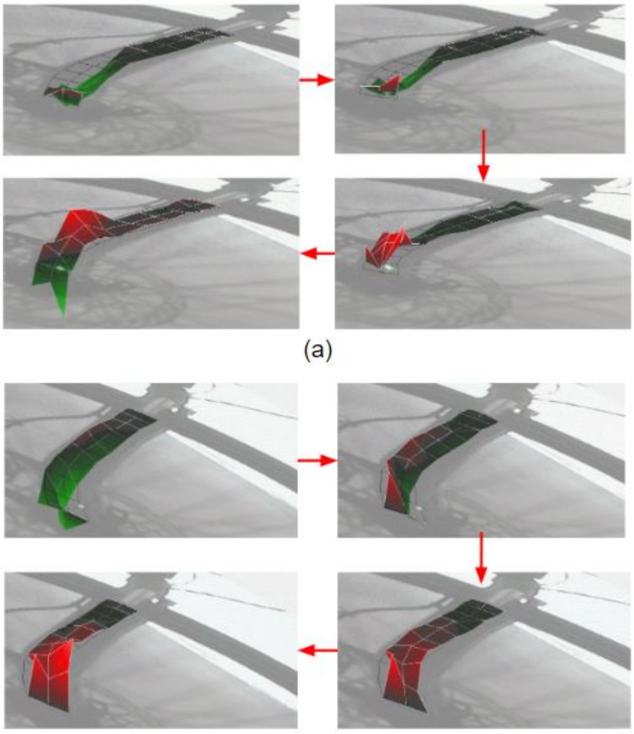
(a)

(b)

Figure 4.5: Mode shapes of the fork scanned by laser Doppler vibrometer during the brake noise event, the green and red areas denote the positive and negative displacements of the fork, the arrows denote the order of snippets that reveals how the deformations travel in the fork during (a) Chatter: 587 Hz, (b) Squeal: 1176 Hz

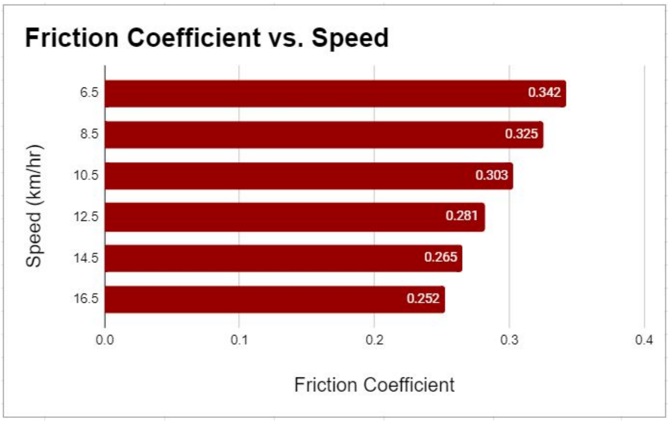

Figure 4.6: Decreasing friction coefficient of the frictional surface with the increasing cycling speed

wet weather conditions. The water might lower the temperature at the sliding interface by the process of evaporation. The temperature dependence of chatter and squeal, however, was not studied in this present project.

The dynamic characteristics of the vibrating bicycle components were studied using the laser Doppler vibrometer. The vibrometer scans shed light on both the brake noise and no noise events. For the brake noise events the vibrometer Magnitude Vs. Frequency plots correlated highly with the audio Amplitude Vs. Frequency plots. This shows that the brake components are vibrating at the exact same frequencies of the noise that an observer hears. It was observed that under the brake noise events, the rotor vibrated the most at more than 1.5 mm/s, the caliper vibrated at a little less than 1.5 mm/s, and the front fork vibrated at 400μm/s. This confirms that the rotor-pad interface is indeed the source of the vibrations as the maximum vibrations are observed for the rotor. The vibrations originate from the sliding interface and propagate from the brake system to the hub and from the hub to the front fork. The vibrations damp down as they travel away from the source as captured by the vibrometer frequency plots (see Figure 4.2). Therefore, during the brake noise events, the entire bike vibrates at three peak frequencies but the sound is emanated from the pad-rotor sliding interface. It is also observed from Figure 4.2 that the maximum out-of-plane vibrations for the bicycle components lie in the chatter region (550-650 Hz). Squeal had lesser out-of-plane vibration amplitude in both wet and dry conditions than chatter (see Table 4.2) even though the chatter noise reduces under wet conditions (see Table 4.1). This means that the higher frequency vibrations do not propagate as much as lower frequency vibrations throughout the brake assembly.

The mode shapes of the fork in chatter had less twist and more out-of-plane motion, whereas the fork in squeal had more twist and less out-of-plane motion. This suggests that during a brake noise event the fork vibrates both in the bending and torsional directions. The fork also did not have significant vibration amplitudes at higher frequencies.

The vibration amplitude of the bicycle components was found to be higher under the wet weather conditions in all three frequency regions (see Table 4.2. Also, under dry conditions the brake noise generation was rather random and certain test runs did not produce any brake noise at all. This suggests that wet weather conditions are worse than the dry conditions when it comes to brake noise and vibrations.

The dynamic friction coefficient was found to be decreasing with an increase in the bicycle running velocity. This observation reveals the presence of stick-slip as one of the causes of friction-induced instabilities in the brake system, which leads to an increase in the vibration amplitude of the brake components. Stick-slip explains the randomness of the brake noise and why the brake noise is consistent under the wet weather condition. During wet conditions, a wet film is developed in between the sliding surfaces, which leads to a drop in the friction coefficient and the fluctuation in the tangential directions are larger than in the dry conditions [6]. During dry conditions the drop in friction coefficient is not as consistent and the tangential fluctuations at the interfacial surfaces are also less. This explains why the brake system has more amplitude of vibration under wet weather conditions. Therefore, the brake noise events are the events where the stick-slip causes friction-induced self-excited vibrations in the brake system and the no-noise events are the dry events where the stick-slip is absent.

5

Finite Element Simulations

The Finite Element Method (FEM) is a powerful technique to calculate approximate solutions to complex problems. Bicycle disc brake noise falls under the category of such complex problems to which the finite element method can be applied to find the answers to. This method is an intuitive and straightforward way to generate the governing equations of motions for the disc brake components. The accuracy of the model is usually controlled by the user where the approximations can be refined to simulate the braking response as close as possible to the real-life conditions with a high degree of fidelity.

One of the main purposes of the project was to develop an finite element model of the disc brake to simulate the frictional sliding and obtain the dynamic characteristics of the disc brake components.

5.1. Pre-stressed Modal Analysis

Real life braking systems work under a constant stress state because the friction pads constantly pressed against the rotating rotor. When performing a modal analysis on such systems it is important to capture the pre-stress effect since it changes the natural frequencies of the structures in the system. Tuning of the guitar strings is one of the common examples where the pre-stress affects the mode frequencies.

It is known that the mode frequencies and shapes depend upon the mass and stiffness distribution in the structure.

$$\omega = \sqrt{\frac{K}{M}} \tag{5.1}$$

When a structure is under stress, its stiffness changes due to stress stiffening. This stress alters the vibrational characteristics of the structure, the new natural frequency of the structure is

$$\omega = \sqrt{\frac{K+S}{M}} \tag{5.2}$$

where **S** is the stiffness matrix. The derivation of stress matrix in the stiffness matrix is discussed in detail in Appendix D

5.2. Method of Analysis

To perform a pre-stressed modal analysis, the first step is to perform a base stress analysis. The base stress analysis can either be static or transient analysis also it can either be linear or non-linear analysis. During the linear analysis the stress stiffness matrix **S** is computed and in case of non-linear analysis the changes in mass **M** and stiffness **K** matrices are also captured. During the braking simulations the mass of the system may not change but the changes in the center of gravity because of the deformations in the brake components are captured in the base stress analysis. If the base stress analysis is linear then the eigen frequencies are calculated using the undeformed mesh and if the base stress is a non-linear analysis, the deformed mesh is used to calculate the eigen frequencies.

In Ansys pre-stressed modal analysis is performed by first creating the structural analysis block. The solution from the structural analysis is input to the modal analysis block and the links between the two blocks are automatically created.

For the present study the FE analysis are performed on ANSYS Workbench 2021-R2 software. The natural frequencies and the mode shapes computed from the simulations are compared with the experimental results from chapter 4.

5.3. Limitations of Analysis

The limitations of the present analysis are as follows

5.3.1. Reduced Model

The FE model used in the analysis is a reduced model consisting of only a rotor, brake pads, and the caliper. The rotor and brake pads are modeled as close as possible to the original parts but the caliper model is a highly simplified design of the original model. Unlike the rotor and brake pads design, the caliper model has no geometric similarities to the original part used in the experiments. The finite element caliper model does not have the intricate details like shims, bolts, pins, pistons seals, mounting brackets, biasing member, actuation unit, pad axle, hydraulic through holes, and hydraulic connections, it only consists of a caliper body and two pistons. The material properties used in the rotor, brake pads, and the caliper for the analysis also differed a bit from the original components as these values are hard to get. Shimano on their website [11] mentions the three layered rotor material (Stainless steel-Aluminium-Stainless steel) as shown in Figure 5.1, which was not reproduced in the finite element model. The finite element model had stainless steel as the only material assigned to the backplate and the rotor. This is a reasonable assumption because the real rotor and backplate components have stainless steel as the majority of their material. Table 5.1 shows the material properties of the frictional lining used in the finite element simulations. The frictional lining was simplified to have a smooth surface with no asperities.

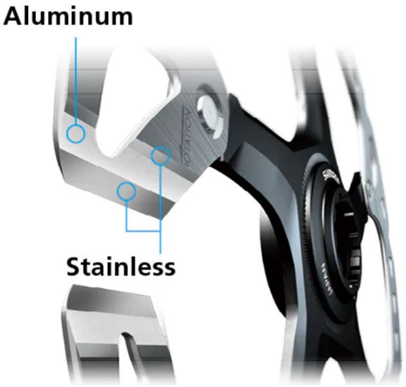

Figure 5.1: Shimano rotor material layers for better heat conduction and performance [5]

5.3.2. Limited degrees of freedom

The model had to limit the degrees of freedom of brake components for simplicity and computational purposes. The brake pads were only allowed to move in the direction normal to the brake pad surface to allow the pads to travel along with the piston as the piston presses against them. Therefore, for the pads only the degrees of freedom in the direction normal to the pad-rotor interface were retained. Although it is well documented that a change in the center of pressure (COP) at the brake pad can alter the brake noise propensity and generation [8], the present finite element model has the constraints applied to its leading and trailing edge to ensure a constant pressure distribution at the pad-rotor interface.

Brake material	
Density	2045 kg/m3
Young's Modulus	2.6e+09 Pa
Poisson's Ratio	0.34
Bulk Modulus	2.7083e+09 Pa
Shear Modulus	9.7015e+08 Pa
Yield Strength	2.5e+08 Pa

Table 5.1: Structural material values for the brake pad friction lining used in FEA simulations

During a real life braking event, the COP providing the force normal to the disc surface, generated by caliper piston varies considerably and is offset from the centerline of the caliper mounting arrangement. This offset of COP happens because of the degrees of freedom of the brake pad and the element of elasticity at the sliding surfaces. Figure 5.2 shows the disc brake system components where 'A' is the brake pad, 'B' is the caliper axle pin, 'C' is the piston, and 'D' is the rotor. The brake pad rests on the axle pin while the caliper piston pushes it against the rotor. In actual braking scenario the brake pad has four degrees of freedom at 'B' i.e. the three translations in in X, Y, and Z and a rotation around Z. The rotations around X and Y are restricted by the piston and the rotor. Out of the three translations, the translations in X and Y are very small but enough to couple with the rotation around Z and cause an offset in COP. The finite element model does not capture these translations, instead it only has 1 DOF of the brake pad at the axle pin denoted by a prismatic joint in Figure 5.3a. The finite element model does not capture the offset in COP instead there is a uniform pressure distribution over the brake pad during the braking event. Figure 5.3 shows the Free Body Diagram (FBD) of the brake pad with all the constraints and the forces on the pad. Figure 5.3b shows the leading and trailing edge of the frictional lining. Both the leading and trailing edges maintain constant contact with the rotor at all times and the pressure from the piston is equally distributed at the rotor-pad interface. In a real world scenario the pressure ratio of the leading and the trailing edge is dynamic and COP lies more towards the leading edge.

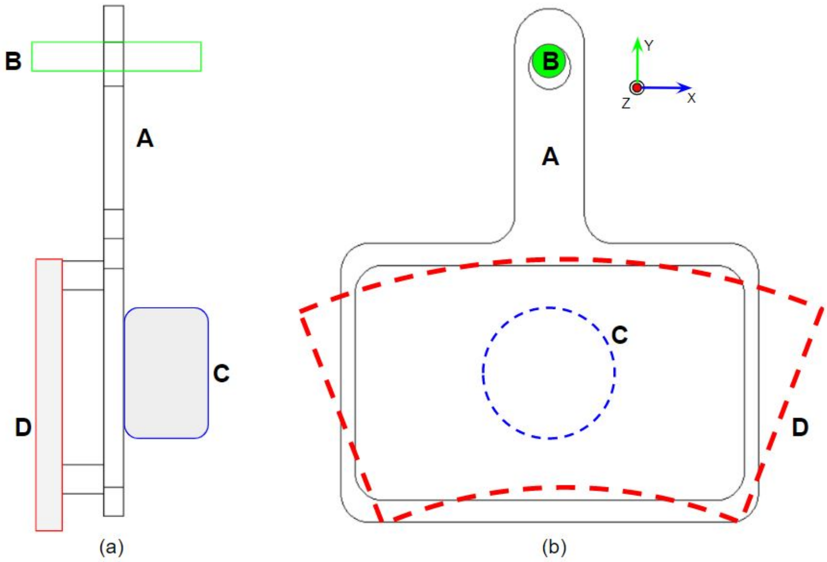

Figure 5.2: FBD of the brake pad with the constraints and the forces (a) Side view of the pad showing a prismatic joint at 'A' and reaction forces from the rotor at 'B', the pressure from piston is applied on the backplate shown by 'C' (b) Front view of the pad shows the frictional lining in green, which presses against the rotor that acts as the fixed support for the lining. The arrow in gray shows the rotor rotation direction and 'T' and 'L' are the trailing and the leading edge

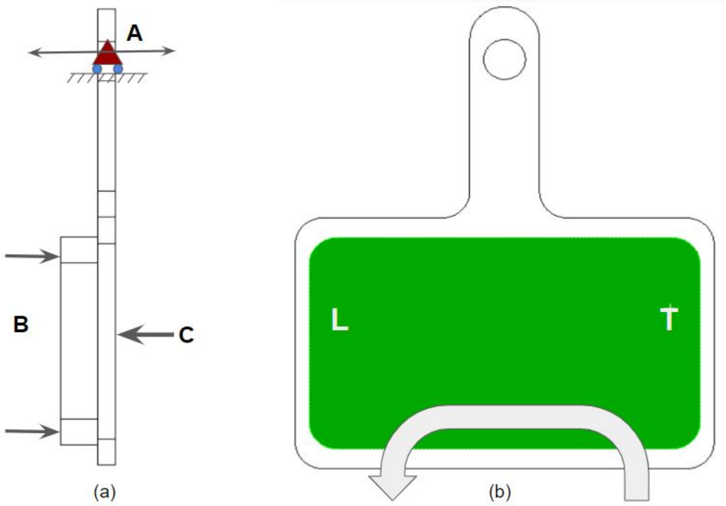

Figure 5.3: FBD of the brake pad with the constraints and the forces (a) Side view of the pad showing a prismatic joint at 'A' and reaction forces from the rotor at 'B', the pressure from piston is applied on the backplate shown by 'C' (b) Front view of the pad shows the frictional lining in green, which presses against the rotor that acts as the fixed support for the lining. The arrow in gray shows the rotor rotation direction and 'T' and 'L' are the trailing and the leading edge

5.3.3. Absence of frictional heating

Frictional heating is one of the by-products of the friction sliding between the rotor and the brake pads. The frictional heating is known to increase the friction coefficient at the interface and the change in friction coefficient is responsible for the instabilities in the pad-rotor interface. Moreover, the improper energy balance also affects the brake noise generation, which this model fails to capture.

5.3.4. No stick-slip

Stick-slip was identified as one of the causes of friction induced vibrations during the experimental investigation. Even though the pre-stress analysis includes the the frictional sliding contact of the pad and rotor, it fails to incorporate the stick-slip effect in the model.
The governing equation of the system without stick-slip is:

$$m\ddot{x} + c\dot{x} + kx = 0$$

The governing equation with the stick-slip effect changes to

$$m\ddot{x} + c\dot{x} + kx = F$$

where F is the forcing function that comes from the stick-slip effect. Modal analysis fails to capture the external forces on the system and thus $F = 0$. Also, stick-slip is a nonlinear phenomenon that is a function of $\dot{x}$ whereas, modal analysis is an inherently linear concept.

5.4. Development of Finite Element Model

The finite element model of the rotor and brake pads for the analysis had the same dimensions as the rotor and pads used in the experimental investigation. The caliper model was a highly simplified model as discussed previously. The finite element model of the disc brake assembly consisted of a rotor, brake pad assembly, caliper, and caliper pistons as shown in Figure 5.4.

The program controlled fine mesh was chosen for the analysis. The loads to the finite element model were applied to the solid model on the surfaces. Normal load was applied on the pistons to simulate the hydraulic pressure onto the backplates of the brake pads. The rotor was given a rotation about the axis normal to the sliding surface. Figure 5.5 shows the loading conditions of the finite element model. The constraints and the loads on the brake pads are shown in Figure 5.3. The rotor was constrained by limiting the DOFs at the hub. Figure 5.6 shows the highlighted green holes on the rotor

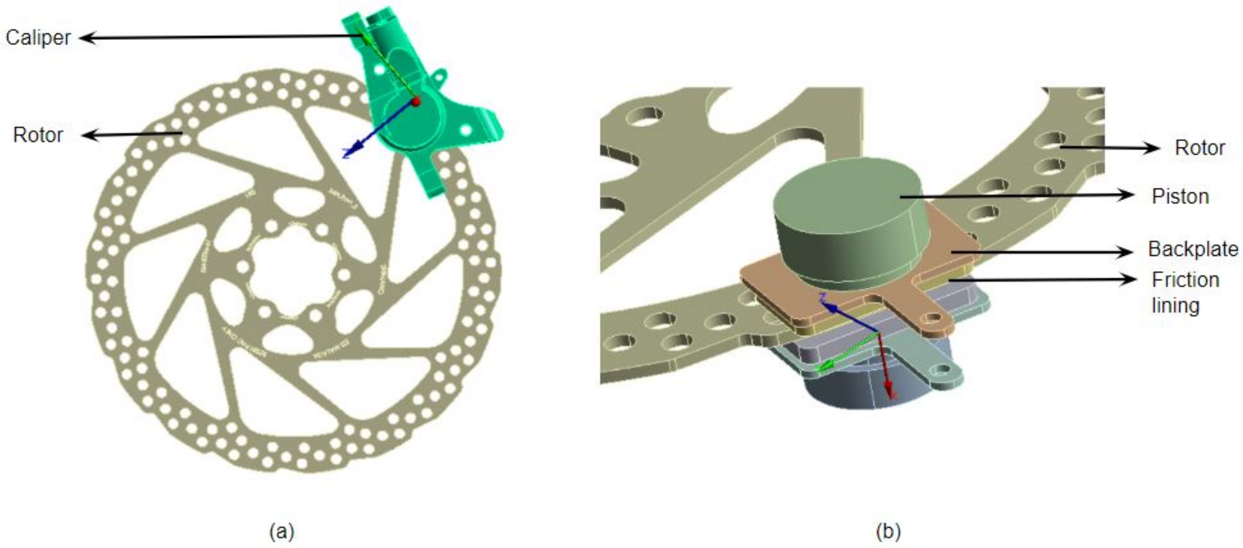

Figure 5.4: Finite element model of the brake assembly (a) Rotor and Caliper (b) Zoomed in Rotor, Caliper pistons, Backplate, and Friction lining

where the constrains were applied. All three translations and the rotations about the Y and X axes were constrained at the hub holes.

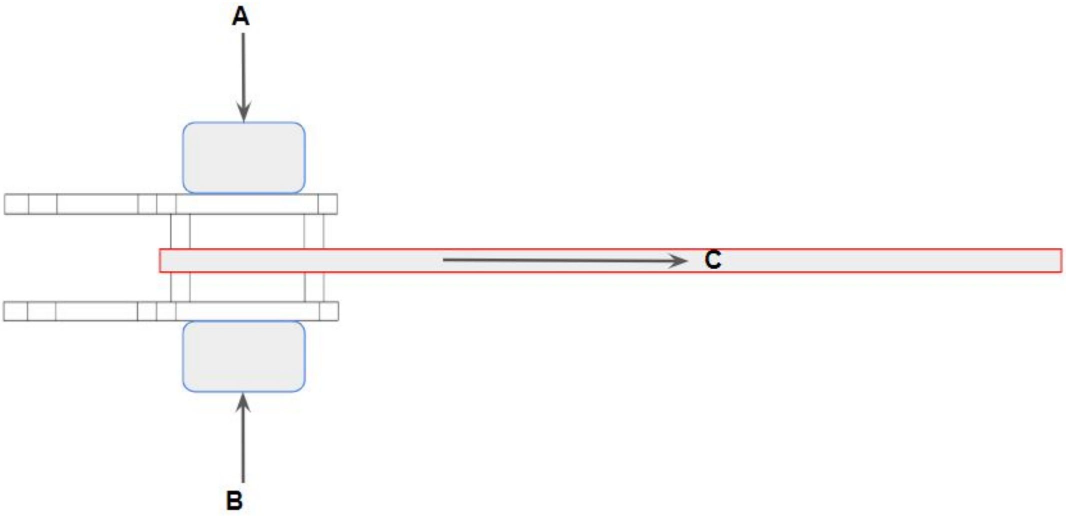

Figure 5.5: Normal loads A and B on the pistons denote the hydraulic pressure by the caliper on the brake pads and C denotes the rotation direction of the rotor that simulates the frictional sliding in the system

5.5. Finite Element Contact Analysis

ANSYS offers three contact algorithms and these are surface to surface, node to node, and node to surface. While defining contacts between different bodies of the model, the surface-to-surface contact model was chosen for the present analysis. In surface to surface type of analysis the contact elements use a ”target surface” and a ”contact surface” to form a contact pair. Surface to surface model provides the best balance between the computational resources to solve the problem and the contact results. Surface to surface model also supports the large deformations and frictional sliding the best. Node-to-surface contact algorithm is generally used to model point-to-surface contact applications, whereas node to node contact algorithm is used to model the point-to-point contact applications.

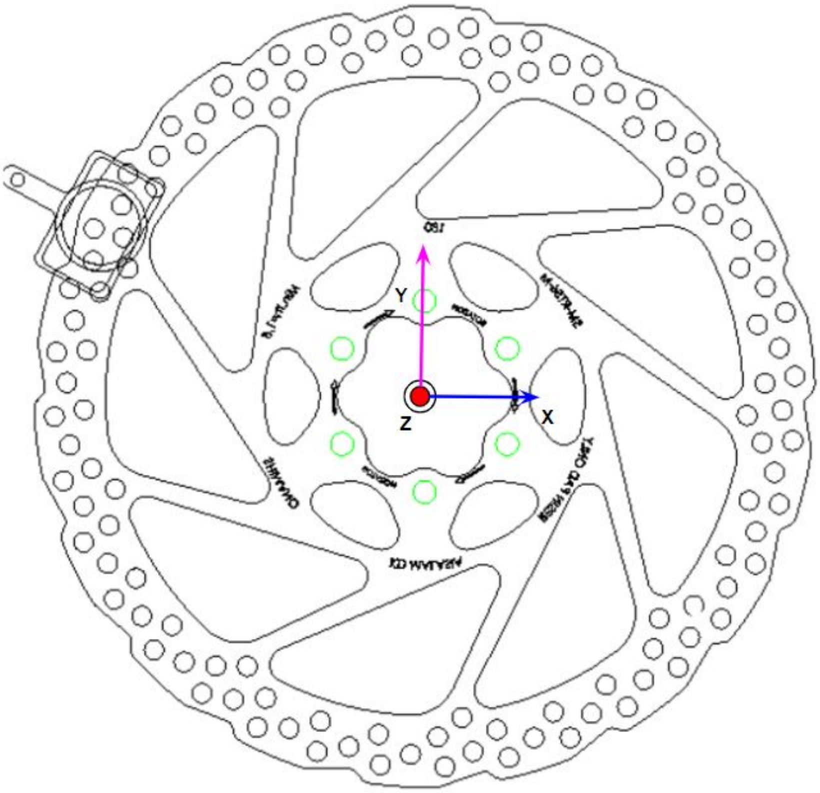

Figure 5.6: Constraints on the rotor at the holes highlighted in green. Only one DOF, which is the rotation about Z axis, was retained and rest five DOF were constrained

ANSYS was allowed to identify and generate automatic contacts between the bodies initially. All the automatic contacts that ANSYS generates are by default bonded contacts. Bonded contacts stick two bodies together and allows no relaive motio between them. The contact type between the caliper body and caliper pistons was set as a frictionless contact to allow a smooth motion between the surfaces. The frictional lining was bonded to the backplates of the brake pads. The pistons and brake pads shared a bonded contact type. For the sliding contact between the two rubbing surfaces, it was identified by Ioannidis [12] that an open gap between the two sliding surfaces represented an un-burnished state of the frictional lining's surface while the closed gap between the frictional lining and the rotor represented a fully worn state. Therefore, the brake pad frictional lining and the rotor were assigned a frictional contact with the initial gap between them closed. For frictional contact, friction coefficient value from the experiments($\mu = 0.3$) was used.

All the components had different material properties and some of the bodies like frictional lining were softer than the other contacting bodies. In ANSYS simulations, contact occurs when the contact elements penetrate the target elements. Therefore, the rotor was defined as the target surface because of its higher stiffness, and the pad friction material was defined as the contact surface.

ANSYS uses the Newton-Raphson approach to solve nonlinear contact problems. The analytical interpretation of this method is discussed in detail in Appendix D.

5.6. Modal Analysis

Modal analysis of the rotor was carried out without any pre-stress to investigate the natural frequencies of the individual component. The rotor was simulated with a fixed boundary condition as discussed in the Figure 5.6. Modal analysis of the brake pad was carried under a pre-stressed condition with the forces and constraints on the brake pad applied as discussed in above sections. Modal analysis of the caliper alone was not conducted because of a highly reduced finite element caliper model, which had no similarities to the real part used in the experiments.

On the entire brake assembly as shown in Figure 5.4, pre-stress modal analysis was performed. Newton-Raphson method was utilized by ANSYS to solve the unsymmetric matrices produced due to the frictional sliding. The addition of stress matrix to the stiffness matrix in the base stress analysis made the structural system non-linear (more on the pre-stress non-linearities are discussed in Appendix D), which was converted by ANSYS to a linear system by default and the mode shapes and natural frequencies were then extracted. The natural frequencies up to 2 kHz were extracted because it is known from the experiments that the range of brake noise for the bicycle brake system is 0 - 2 kHz.

5.7. Summary

This chapter detailed the process of construction of the finite element method of the disc brake assembly to investigate the viability of the numerical simulation techniques to predict the brake noise frequencies. The limitations of the FEA study and the contact analysis including the load cases on the FE model are discussed. A pre-stressed modal analysis route was examined to capture the frictional sliding at the pad-rotor interface. This section also examines in detail the background theory of the addition of stress matrix to the stiffness matrix, which ultimately induces the non-linearities in the system.

6

Finite Element Simulation Results

The finite element model developed in chapter 5 is used to investigate the vibration characteristics of the brake assembly. The results from the simulations are then compared to the results from the experiments to validate the FEA model.

6.1. Modal analysis of the individual components

The results from finite element modal analysis of the rotor and the brake pad are discussed and some key conclusions are made in this section.

6.1.1. Brake pad

A pre-stressed modal analysis on the brake pad was performed as discussed in the previous chapter. The results of the base stress analysis are presented in Figure 6.1. The deformations show that COP is at the center as the maximum deformation is at the center of the pad. The pressure distribution is uniform at the trailing and the leading edge as it can be seen by the symmetrical colour gradient distribution on the model. Modal analysis of the brake pad revealed only one eigen frequency in the region of 0-2000 Hz. The vibration mode as shown in Figure 6.2 vibrated in-plane at 1193.2 Hz and lied in the squeal region.

6.1.2. Rotor

The modal analysis results of the rotor had nine eigenmodes in the range 0-2000 Hz as shown in Table 6.1. Out of these nine eigenmodes, six modes form doublet mode pairs close to the chatter, squeal, and high-frequency squeal regions.

The first two eigen modes of the rotor form the chatter doublet with an out-of-plane frequency close to 575 Hz. Both modes had a mode shape of (2,1) and are shown in Figure 6.3.

Mode	Frequency (Hz)	Description
1	572.78	Mode shape: (2,1) Chatter Doublet
2	579.55	
3	993.35	Mode Shape: (3,1) Squeal Doublet
4	993.93	
5	1551.5	Mode Shape: (4,1) High freq. Squeal Doublet
6	1552.5	
7	1822.6	Mode Shape: (0,2)
8	1974.5	Mode Shape: (1,2) Doublet
9	1983.7	

Table 6.1: Eigen frequencies of the rotor between 0-2000 Hz consisting of doublet modes close to chatter, squeal, and high frequency squeal regions

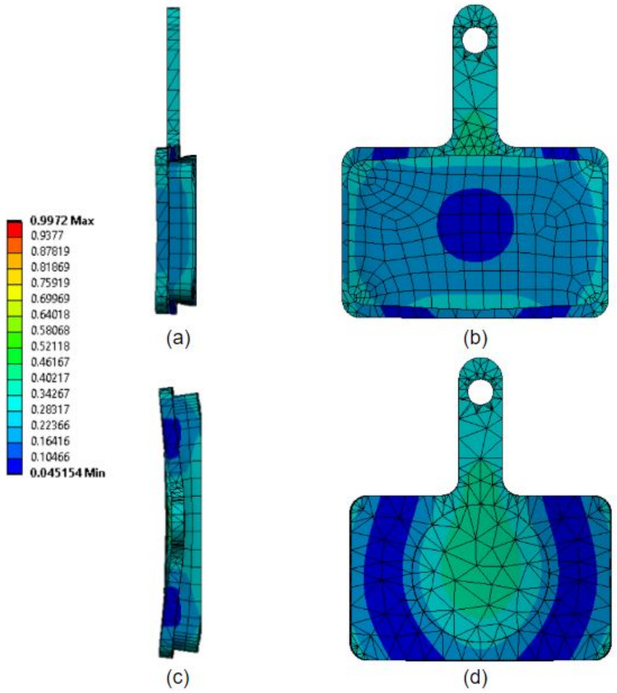
0.9972 Max
0.9377
0.87819
0.81869
0.75919
0.69969
0.64018
0.58068
0.52118
0.46167
0.40217
0.34267
0.28317
0.22366
0.16416
0.10466
0.045154 Min
(a)
(b)
(c)
(d)

Figure 6.1: Deformations on the brake pad as a result of base stress analysis on the brake pad (a) Side view, (b) Front view, (c) Top view, (d) Back view

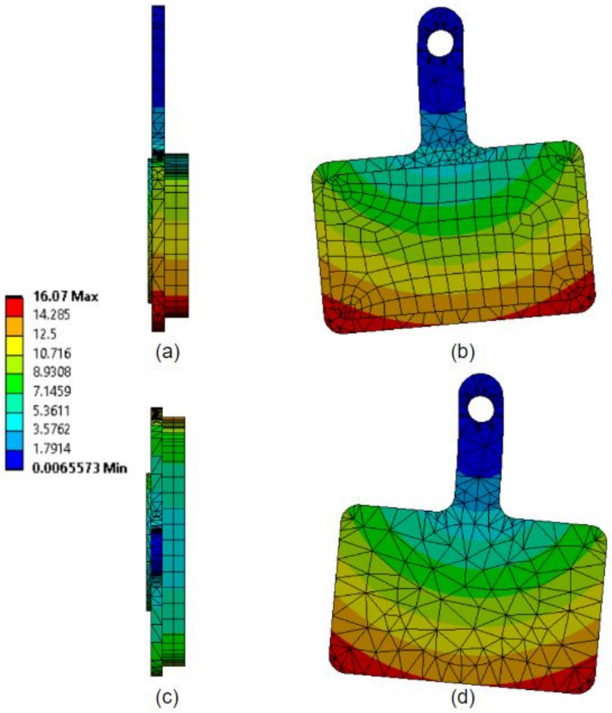
16.07 Max
14.285
12.5
10.716
8.9308
7.1459
5.3611
3.5762
1.7914
0.0065573 Min
(a)
(b)
(c)
(d)

Figure 6.2: Eigen mode of the brake pad in the 0-2000 Hz is the in-plane mode vibrating at 1193.2 Hz (a) Side view, (b) Front view, (c) Top view, (d) Back view

Mode 3 and mode 4 formed the second doublet mode of the rotor. The second doublet lied closer to squeal region with a frequency around 1000 Hz. Mode 3 and mode 4 had the out-of-plane frequencies of 993.35 Hz and 993.93 Hz respectively. Figure 6.4 shows the squeal doublet with the mode shape (3,1). The third doublet close to high frequency squeal region consisted of mode 5 and mode 6 with

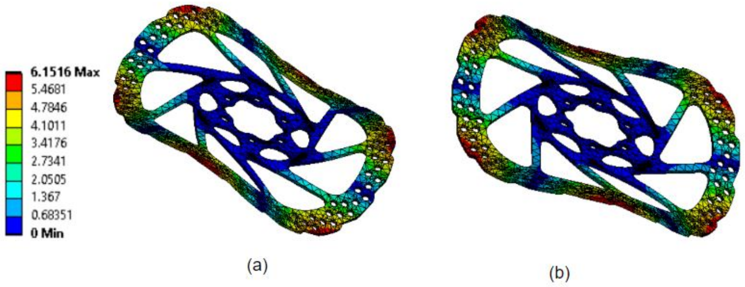

Figure 6.3: Chatter doublet mode (2,1) of the rotor with eigen frequencies close to 575 Hz (a) First mode of vibration of rotor at 572.78 Hz (b) Second mode of vibration of rotor at 579.55 Hz

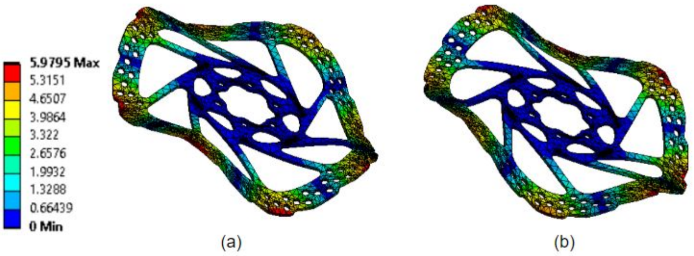

Figure 6.4: Squeal doublet mode (3,1) of the rotor with eigen frequencies close to 1000 Hz (a) Third mode of vibration of rotor at 993.35 Hz (b) Fourth mode of vibration of rotor at 993.93 Hz

the mode shape (4,1). High frequency squeal doublet is shown in Figure 6.5 with a frequency close to 1550 Hz. The remaining three eigen modes of the rotor are shared in Figure 6.6. Mode 7 had the mode shape of (0,2), mode 8 and mode 9 also formed a doublet with the shape of (1,2). The eigen frequencies of the rotor lie close to the regions of Chatter, Squeal, and High-frequency Squeal. The modes of the rotor do not follow the strict frequency ratios as observed during the experiments. The three unstable eigen modes with the mode shapes of (2,1), (3,1), and (4,1) as identified during the experiments were present as the doublet modes in the rotor.

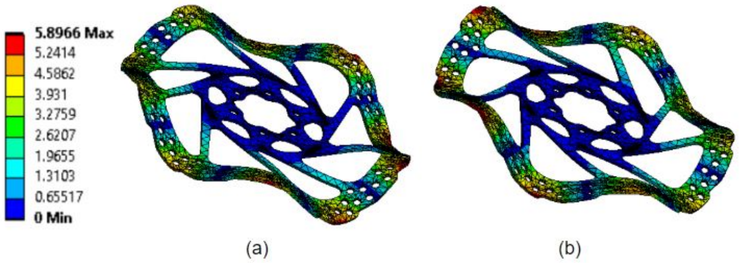

Figure 6.5: High frequency squeal doublet mode (4,1) of the rotor with eigen frequencies close to 1550 Hz (a) Fifth mode of vibration of rotor at 1551.5 Hz (b) Sixth mode of vibration of rotor at 1552.5 Hz

6.1.3. Summary

The component level modal analysis revealed that there exist three frequency regions for the rotor. The frequency regions of both the components lie close together and can couple to vibrate at a higher amplitude. This coupling is called *intermediate modal coupling*. Other than just the *intermediate modal coupling*, which happens between the two different components, the rotor also showed the existence of the doublet modes that causes flutter instability in the system.

The finite element model was correctly able to predict the in-plane eigen frequencies and the mode shapes of the components, which is in accordance with the study conducted by Nakae et al [16] who were able to experimentally observe the in-plane modes in the regions of squeal and high-frequency

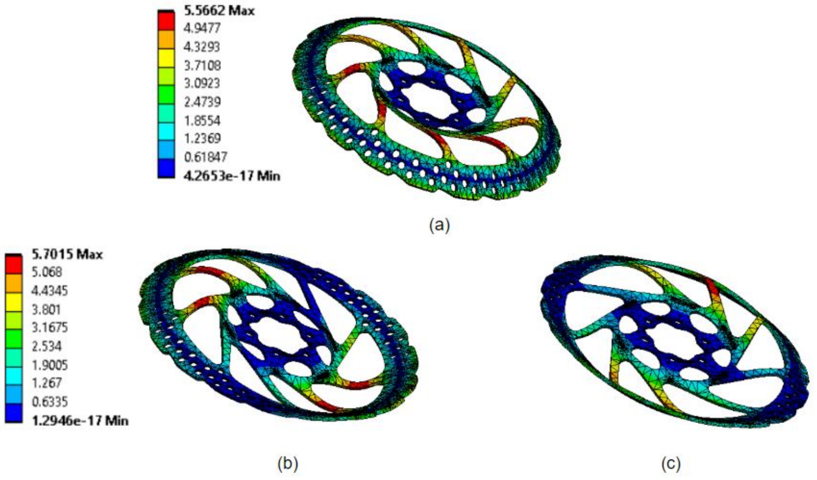

Figure 6.6: (a) Mode 7 of the rotor with the shape (0,2) vibrating at 1822 Hz (b) Mode 8 of the rotor with the shape of (1,2) at 1974 Hz (c) Mode 9 of the rotor with the shape of (1,2) at 1984 Hz

squeal.

6.2. Pre-stressed modal analysis of the disc brake assembly

The base stress analysis successfully simulated the frictional sliding contact at the pad-rotor interface. Figure 6.7 shows the stresses in the brake assembly as a result of pressure from the pistons. A closer view of the brake pad and the rotor in Figure 6.8 also shows a shear stress in the friction lining as a result of sliding and the hydraulic pressure. The stresses in the system are as expected.

Mode	Frequency (Hz)	Description
1	543.75	Mode shape: (2,1)
2	732.12	Mode shape: (2,1)
3	943.5	Mode Shape: (3,1)
4	1072	In-plane mode
5	1167	Mode Shape: (3,1)
6	1510.1	Mode Shape: (4,1)
7	1811.3	Mode Shape: (0,2)
8	1827.5	Mode Shape: (4,1)
9	1864.2	In-plane mode

Table 6.2: Eigen frequencies of the brake assembly after pre-stressed modal analysis; red rows indicate chatter doublet, blue rows are the squeal doublet, and the green rows are the high-frequency squeal doublet

A total of nine eigenmodes were observed in the finite element simulations as shown in Table 6.2. Six eigenmodes (mode 1, mode 4, mode 5, mode 7, mode 8, and mode 9) of the pre-stressed finite element model were observed in the chatter, squeal, and high-frequency squeal regions. The remaining three modes were the doublet modes. As seen in Figure 6.15 mode 1 and mode 2 form a doublet mode. Both the modes have a mode shape (2,1) but a different phase. Similarly, mode 3 and mode 5 form the second doublet mode with the mode shape (3,1). The third doublet mode observed was between mode 6 and mode 8.

Only one eigen frequency was observed in the chatter range. The chatter mode vibrated in an out-of-plane direction at 545 Hz as shown in Figure 6.9. There were two modes observed in the squeal region that were present within 100 Hz of each other. Out of the two squeal modes, one of the modes was in the out-of-plane direction vibrating at 1167 Hz and the other one was in the in-plane direction vibrating at 1072 Hz as shown in Figure 6.10.

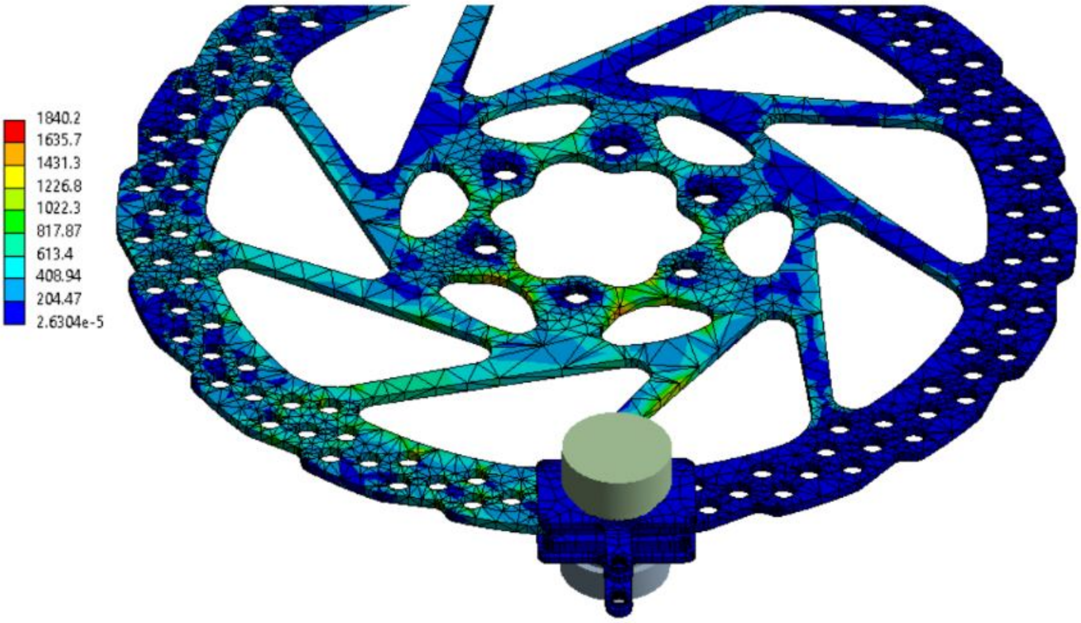
1840.2
1635.7
1431.3
1226.8
1022.3
817.87
613.4
408.94
204.47
2.6304e-5

Figure 6.7: Base stress structural analysis for the pre-stress modal analysis showing the stresses in the rotor and the pads as a result of the hydraulic pressure by the pistons on the brake pads

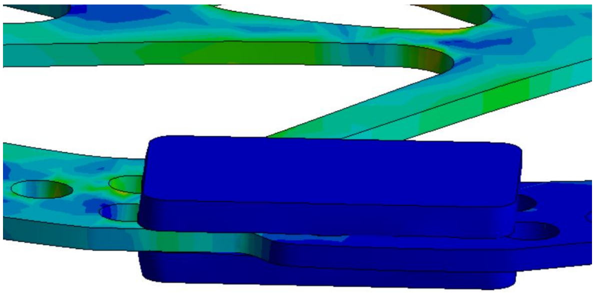

Figure 6.8: Base stress analysis showing shearing of the brake lining because of the friction and the hydraulic pressure

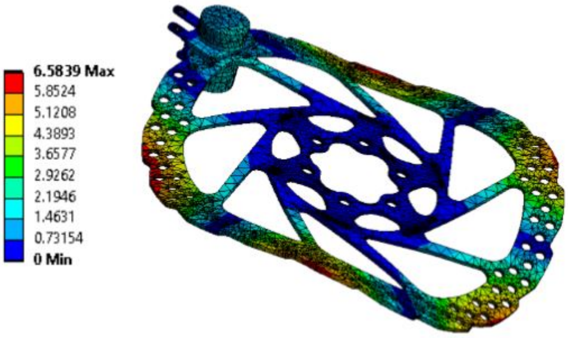
6.5839 Max
5.8524
5.1208
4.3893
3.6577
2.9262
2.1946
1.4631
0.73154
0 Min

Figure 6.9: Brake assembly pre-stressed eigen mode in the chatter region vibrating at 545 Hz in the out-of-plane direction

Under the high-frequency squeal regions, three eigen modes were observed vibrating at 1811 Hz, 1830 Hz, and 1864 Hz. The first two modes were in out-of-plane direction and the last mode was in the in-plane direction as shown in Figure 6.11.

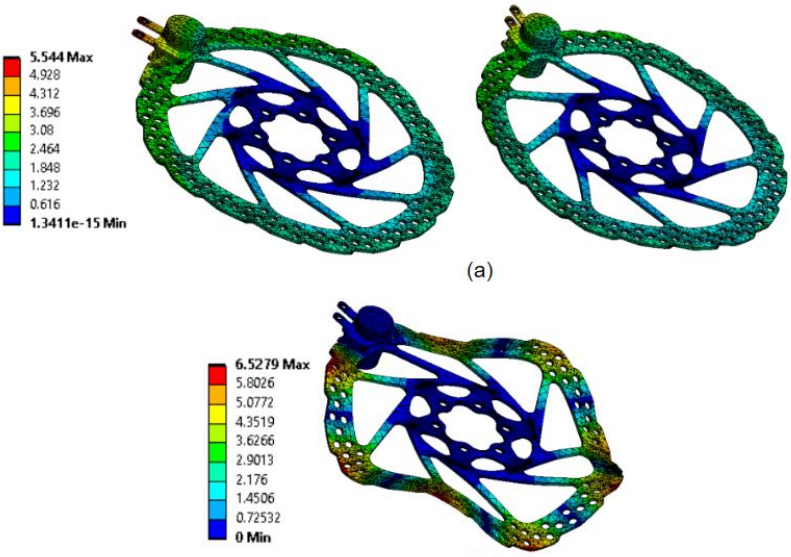
5.544 Max
4.928
4.312
3.696
3.08
2.464
1.848
1.232
0.616
1.3411e-15 Min
6.5279 Max
5.8026
5.0772
4.3519
3.6266
2.9013
2.176
1.4506
0.72532
0 Min

(a)

(b)

Figure 6.10: Brake assembly pre-stressed eigen modes in the squeal region (a) In-plane mode at 1167 Hz, (b) Out-of-plane mode at 1072 Hz

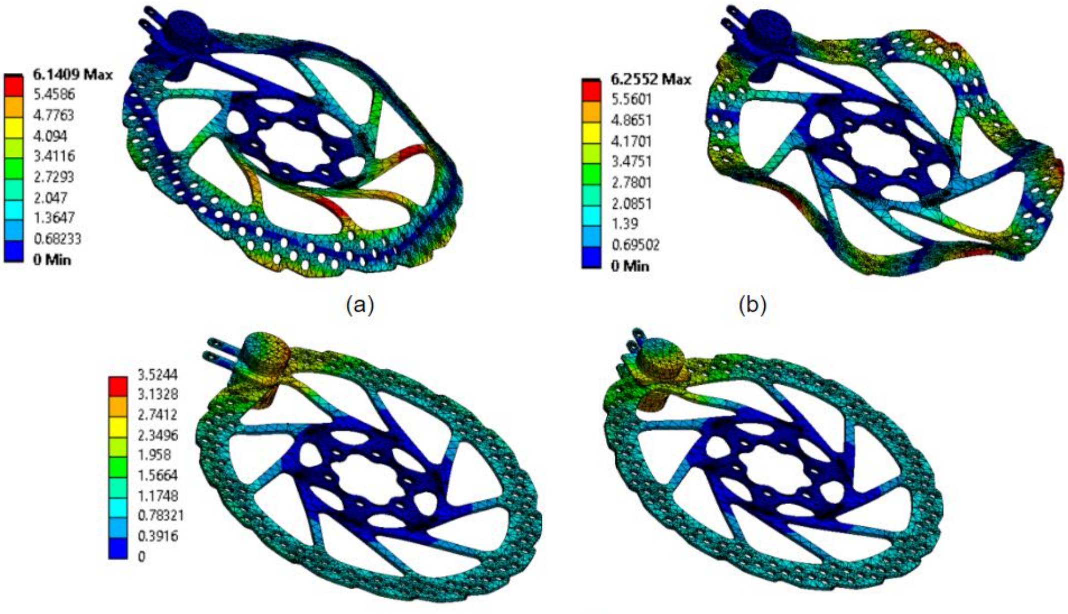
6.1409 Max
5.4586
4.7763
4.094
3.4116
2.7293
2.047
1.3647
0.68233
0 Min
6.2552 Max
5.5601
4.8651
4.1701
3.4751
2.7801
2.0851
1.39
0.69502
0 Min
3.5244
3.1328
2.7412
2.3496
1.958
1.5664
1.1748
0.78321
0.3916
0

(a)

(b)

(c)

Figure 6.11: Brake assembly pre-stressed eigen modes in the high frequency squeal region (a) First out-of-plane mode at 1811 Hz, (b) Second out-of-plane mode at 1830 Hz, (c) In-plane mode at 1864 Hz

6.3. Comparison with the experimental Results

The investigated brake system consisted of two sliding components in focus, i.e. the brake pads and the rotor. The dynamics (natural frequencies, and vibration modes) of both the components were found out when they were considered separately. It was observed that the assembly of the components when coupled through a friction interface had different frequencies and modes from the components when they were considered separately. This is because of a change in the dynamics due to the non-linear pre-stress and the frictional coupling in the system, which changes the stiffness, mass and hence, the overall natural frequencies of the system.

The frequencies of the brake assembly lied in between the frequencies of the brake pad and the rotor.

The friction coupling between the two components causes them to vibrate at a natural frequency that lies in-between or close to the natural frequency of either component known as intermediate mode lock-in [[3]]. Therefore the frictional coupling between the components, the intermediate mode lock-in, and the prestress in the system is the reason the eigen frequencies of the components considered separately differ from the eigen frequencies of the whole assembly coupled together.

The experimental modal analysis using the laser vibrometer provides ample evidence for comparison with the finite element analysis. As mentioned before, the rotor and the brake pads modeled in the analysis were dimensionally very similar to those used in the experiments, thus a direct comparison can be made.
The results from the finite element simulations and the experiments were compared based on the eigen frequencies and vibration modes. The dynamics of the system for the two types of analysis correlated well and were almost similar. While the experimental runs provide only the end result, the finite element analysis sheds more light on why some of the things that were observed experimentally could be happening. In a way both the analysis types complemented each other well. From the experiments, it was observed that there existed only three peak frequencies during the brake noise events whereas the finite element simulations showed the presence of more than three frequencies in the assembly. One of the reasons for this difference in the number of eigen frequencies between the two analysis types is that the in-plane modes were not studied experimentally but were found out in the finite element study. Also, no doublet modes were observed in the experimental study, which is another reason for an increase in the number of eigen frequencies in finite element analysis. Of all the nine frequencies identified via finite element simulations, six could be grouped together into the three regions i.e. chatter, squeal, and high-frequency squeal as shown in Table 6.2. Figure 6.12 shows the mode (2,1) in the range of chatter for experimental and finite element modal analysis.

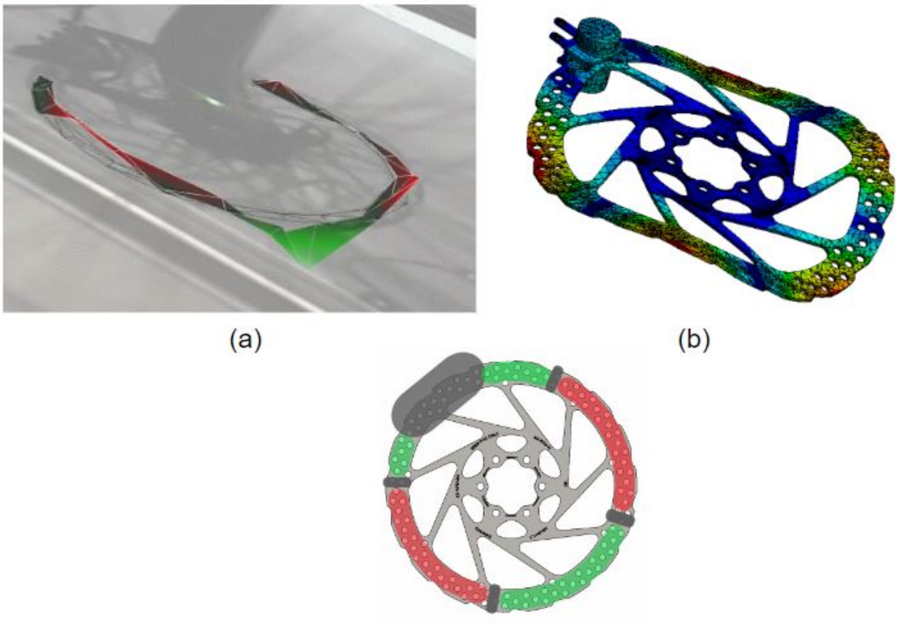

(a) (b)

(c)

Figure 6.12: Mode (2,1) (a) Result of mode shape in chatter from the experiments vibrating at 591 Hz (b) Result of mode shape in chatter from the experiments vibrating at 545 Hz (c) Simple interpretation of the mode shape

Not only were the mode shapes between the two types of analysis similar, but the frequencies from the finite element modal analysis also followed closely to those from the experimental analysis. It was found that the brake assembly was in the chatter at 591 Hz experimentally and at 545 Hz analytically. Figure 6.13 shows the mode (3,1) in the squeal range vibrating at 1190 Hz from the experiments and at 1167 Hz from the finite element simulations.

The mode (4,1) as shown in Figure 6.14 was found in the range of high frequency squeal with a frequency of 1786 Hz from the experiments and with a frequency of 1830 Hz from finite element

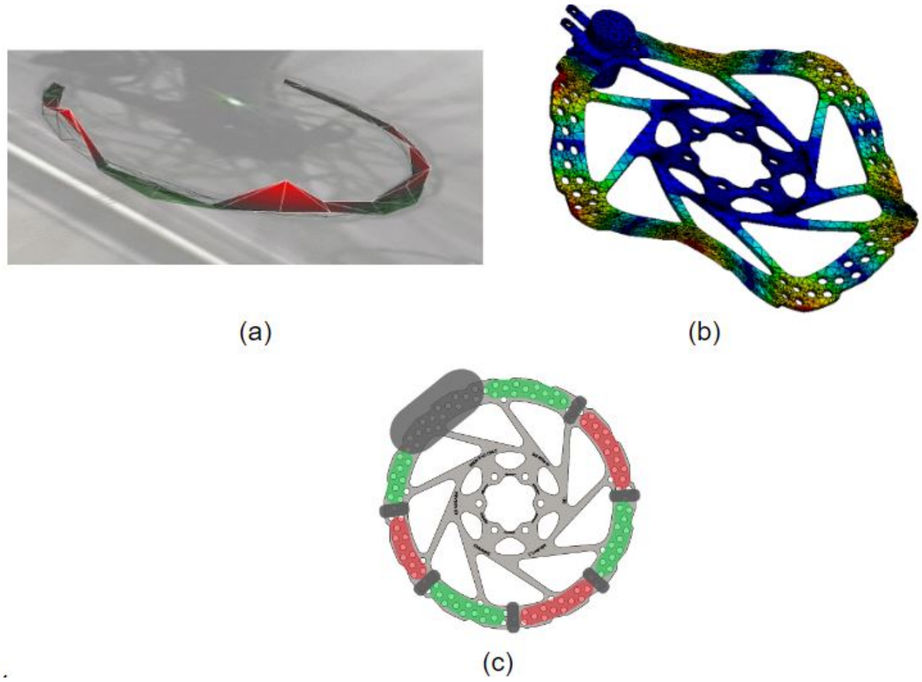

(a) (b)

(c)

Figure 6.13: Mode (3,1) (a) Result of mode shape in squeal from the experiments vibrating at 1190 Hz (b) Result of mode shape in chatter from the experiments vibrating at 1167 Hz (c) Simple interpretation of the mode shape

simulations. Experimentally, bicycle components had the maximum vibration amplitude in the region of chatter, moderate amplitude in the squeal region, and very less vibration amplitude in the high-frequency squeal regions (see Table 4.2). This trend was also observed in the finite element results as shown by the colour-bar scale in the Figures 6.9, 6.10, and 6.11. The similar mode shapes and the frequencies of the modes in the experiments and the finite element analysis in all three peak frequency regions suggest that the finite element model predicts the eigen frequencies of the brake assembly well. The small differences in the frequencies between the experimental and the analytical analysis

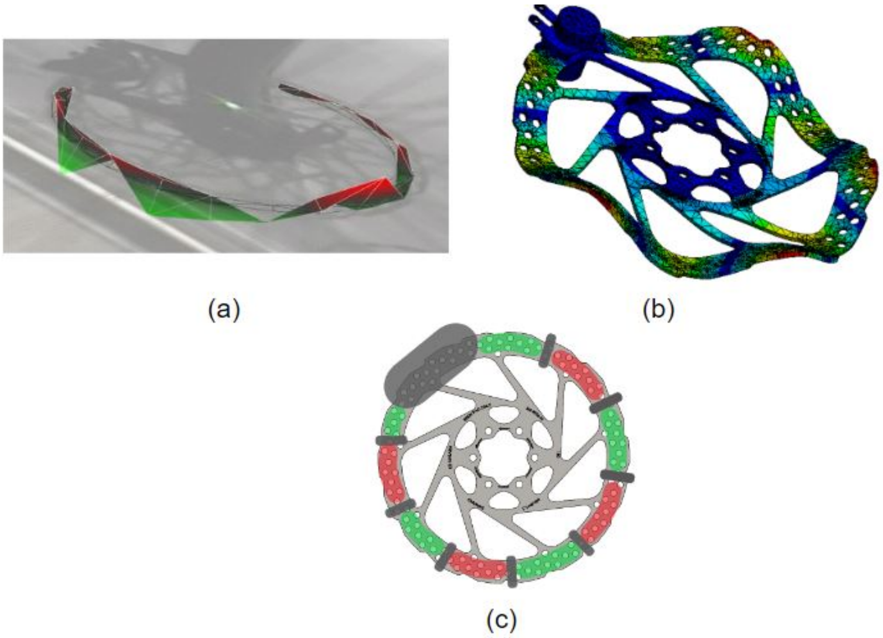

(a) (b)

(c)

Figure 6.14: Mode (4,1) (a) Result of mode shape in squeal from the experiments vibrating at 1786 Hz (b) Result of mode shape in chatter from the experiments vibrating at 1827 Hz (c) Simple interpretation of the mode shape

can be attributed to the limitations of the finite element analysis discussed in the section before. The numerical simulations also found the in-plane vibrating modes in squeal which could not be found via experimental means. Above mentioned observations show that the results from the finite element analysis can be treated with confidence and the finite element model of the disc brake is acceptable for the present purpose of the brake noise analysis.

Figure 6.15 summarizes the eigen frequencies, mode shapes, and the % difference between the experimental and finite element model eigen frequencies.

Mode	Experiments	Mode	FEA	Mode Shape	Mode Shape Interpretation	% Difference
1	**591 Hz**	1	**545 Hz**	(2,1)	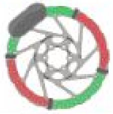	7.70%
	-	2	732 Hz	(2,1)	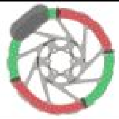	-
	-	3	945 Hz	(3,1)	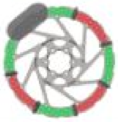	-
	-	4	1072 Hz	In-plane	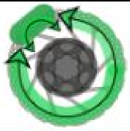	-
2	**1190 Hz**	5	**1167 Hz**	(3,1)	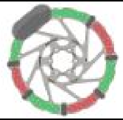	2%
	-	6	1510 Hz	(4,1)	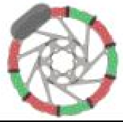	-
	-	7	1811 Hz	(0,2)	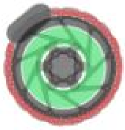	-
3	**1786 Hz**	8	**1827 Hz**	(4,1)	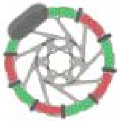	2.30%
	-	9	1864 Hz	In-plane	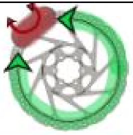	-

Figure 6.15: Summary of the experimental and FEA mode shapes, eigen frequencies and the interpretation of the mode shapes; gray areas are the nodes and the green and red areas are the positive and negative displacements

7

Countermeasures

Based on the observations made during the literature study, experimental investigations, and finite element simulations of the disc brake assembly, three countermeasures were devised to reduce the brake noise magnitude and frequency. The countermeasures were tested experimentally at the Gazelle facility on the brake test machine and also simulated on ANSYS by modeling the simple modifications on the software. This chapter is divided into two sections - Experimental Analysis and Finite Element Analysis. The experimental Analysis section discusses the experimental method of investigation and the experimental results. The finite Element Analysis section discusses how the experimental investigation was reproduced onto the ANSYS software by simplifying the geometry of the brake assembly.

Adnan Akay's [4] comprehensive work on frictional acoustics brought to attention the importance of proper heat balance at the sliding interface to reduce the sound radiations emanating from the interface. To counter the heat conduction problem various automobile brake manufacturers split the friction lining of their brake pads into two halves by means of slots as shown in Figure 7.1. These slots have obvious brake performance advantages; they improve heat dissipation, gas emissions, disc fading, and weight reduction on the brake system [18]. Bicycle brake manufacturers currently do not use slots and holes for their commercial brake pads. Although the smaller size of the bicycle brake pad as compared to the automotive brake pads could be one of the reasons to not use the slots. For the purpose of the present study, a parallel single slot was tested.

Modal analysis of the components revealed that the rotor and the brake pads had close range eigen frequencies. This leads to an intermediate mode coupling that results in an increase in the vibration amplitude. To counter this, the weight of the rotor was increased symmetrically. Increasing the mass of the rotor should decrease its eigenfrequency and that should affect the entire system's dynamics. The interaction of the increased mass of the system with the frictional coupling and the stresses of braking were tested both experimentally and analytically.

The doublet modes were observed in the finite element simulations. These modes lie very close together in the frequency spectrum and often converge together to introduce the system instabilities. Various ways to separate these doublet modes are present in the literature. Lang et al [14] added the mass along the outer circumference of the drum brake and Nishiwaki et al [17] played with the number of stiffeners on the ventilated automotive disc in order to separate the doublet modes. The effect of rotor symmetry plays a huge role in the appearance and convergence of these doublet modes in the structure. In the present study to counter the doublet modes, the mass of the rotor was increased asymmetrically and tested for any improvements in the brake noise magnitude.

7.1. Experimental Analysis

For experimental investigation brake test machine as discussed in chapter 3 was used as the test bench. Gazelle Medeo T10 HMB bicycle and the Magura MT4 caliper and Magura rotor-STORM CL was used in the countermeasure study because the Shimano rotor did not provide enough room for

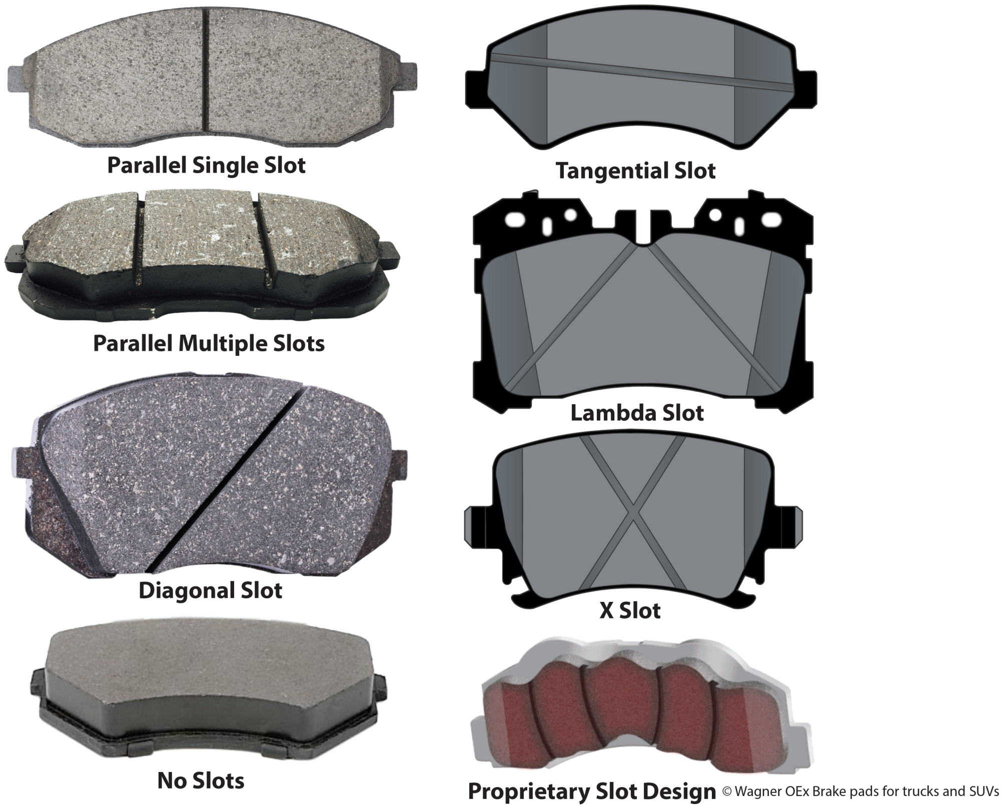

Parallel Single Slot

Tangential Slot

Parallel Multiple Slots

Lambda Slot

Diagonal Slot

X Slot

No Slots

Proprietary Slot Design © Wagner OEx Brake pads for trucks and SUVs

Figure 7.1: Types of brake pad slots used in the commercial automotive vehicles [7]

modifications. The bike was run on the brake test machine at a constant speed of 5 km/hr. A brake force of 80 N at the handlebar, which translated to 263.14 N at the pad-rotor interface was applied. Brake noise audio measurements were taken for the test runs. The experimental test runs are summarized in Table 7.1.

Test Run	Type of Run	Modifications	Audio Measurements	Running Conditions	Weather Conditions
1	Reference	No modifications	Yes	5 km/hr, 80 N	Wet
2	Reference				
3	Reference				
4	Slotted	A parallel slot in the brake pad			
5	Slotted				
6	Slotted				
7	Symmetrically loaded	9 grams mass symmetrically loaded on the rotor			
8	Symmetrically loaded				
9	Symmetrically loaded				
10	Asymmetrically loaded	9 grams mass asymmetrically loaded on the rotor			
11	Asymmetrically loaded				
12	Asymmetrically loaded				

Table 7.1: Summary of the test procedure for the countermeasures with the running conditions and modifications for every case

7.1.1. Reference run

To compare the data and study the effects of countermeasures, a reference run keeping the rotor and brake pads in their original state with no modifications was conducted. For the reference run, rotor mass was measured at 215 grams.

Brake noise audio measurements results are captured in Table 7.3 where the blue rows are the reference run results.

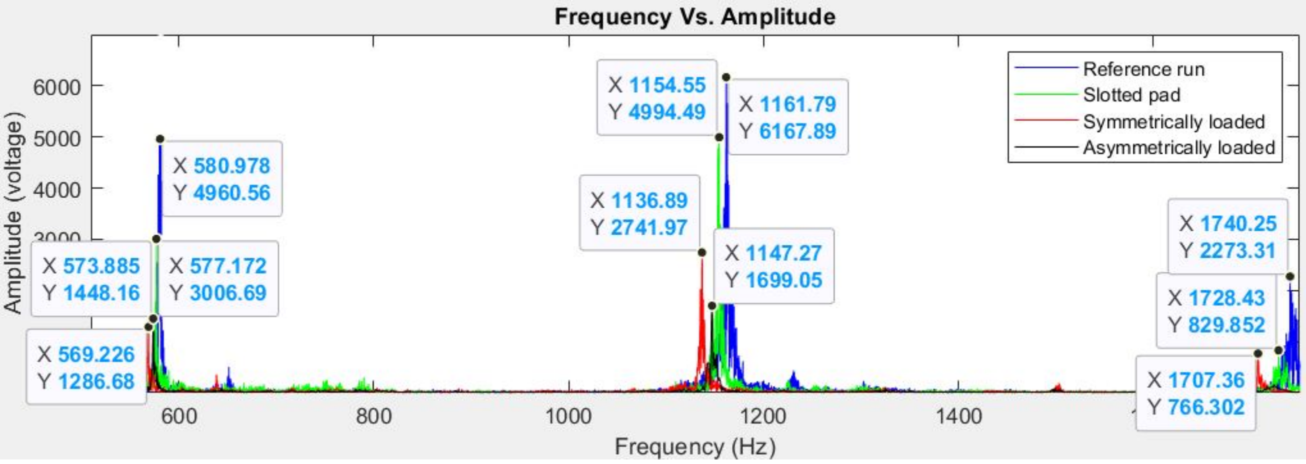

Figure 7.2: Brake noise audio scan of Reference run (Test run 1) in blue, Slotted run (Test run 4) in green, Symmetrically loaded run (Test run 7) in red, and an Asymmetrically loaded run (Test run 10) in black

7.1.2. Parallel slot in the brake pad

To improve the heat conduction a 1.5 mm wide and 2 mm deep parallel slot was made in the friction lining of the brake pad as seen in the Figure 7.3. The slot was created using a file in the middle of lining separating it into to equal halves.

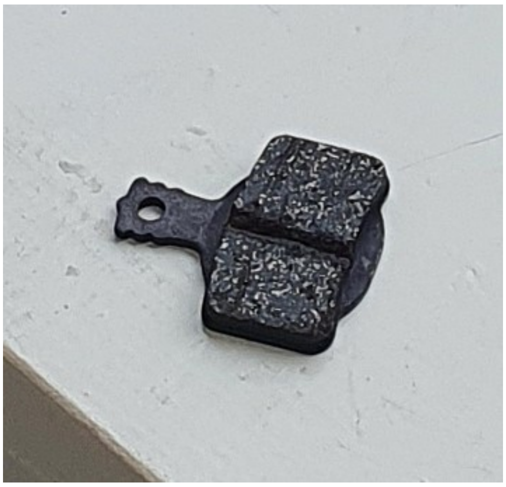

Figure 7.3: 1.5 mm wide and 2 mm deep parallel slot in the friction lining dividing it into two small blocks for better heat conduction

The brake noise audio results are displayed in Table 7.3 where the green rows represent the slotted runs. For comparison, the slotted run (Test run 4) shown in green is plotted against the reference (Test run 1) and the loaded runs (Test run 7 & 10) in Figure 7.2. The change in decibels ΔL of brake noise caused by the parallel slotted brake pad is calculated by

$$\Delta L = 20 \cdot log_{10}(y) \tag{7.1}$$

where y is the ratio of sound pressure field (voltage). Table 7.2 shows the % decrease in the magnitude of brake noise and the change in brake noise decibel levels after using a parallel slotted brake pad. Although the brake noise magnitude decreased by a considerable amount, the brake noise frequencies remained fairly unaffected. The change in braking performance of the slotted brake pad was not investigated. Even though the slot was successful in suppressing the brake noise, its adverse effects on the braking performance if any, were not looked into.

Brake noise	Reference		Slotted		% Magnitude reduction	Decibel change
	Frequency (Hz) (average)	Magnitude (voltage) (average)	Frequency (Hz) (average)	Magnitude (voltage) (average)		
Chatter	580.8	4833.9	581.2	2964.6	38.7	4.2
Squeal	1162.6	6155.5	1159.1	5015	18.5	1.73
High freq. squeal	1740.8	2124.9	1730.3	910.3	57.2	7.35

Table 7.2: Comparison of the brake noise magnitude and frequency of the parallel slotted brake pad with the reference run

Decrease in overall brake noise contribution suggests that parallel slot was able to conduct heat better and improve the heat balance of the system.

Test Run	**Frequency (Hz)**			**Amplitude (voltage)**		
	Chatter	**Squeal**	**High freq. Squeal**	**Chatter**	**Squeal**	**High freq. Squeal**
1	580.9	1161.8	1740.25	4960.5	6167.9	2273.3
2	581.9	1162.8	1741.46	4717.5	6241.0	1783.4
3	579.7	1163.4	1740.87	4823.7	6057.7	2318.1
4	577.2	1154.5	1728.43	3006.7	4994.5	829.8
5	583.8	1171.5	1738.4	2684.8	5265.8	921.8
6	582.8	1151.3	1724.02	3202.3	4784.7	979.4
7	569.2	1136.9	1707.36	1286.7	2741.9	766.3
8	569.2	1139.6	1706.84	1124.8	2799.2	842.9
9	566.7	1138.8	1707	1219.3	2639.0	757.2
10	573.8	1147.3	-	1448.2	1699.0	-
11	576.2	1155.7	-	1374.4	1645.1	-
12	573.3	1148.7	-	1238.9	1663.8	-

Table 7.3: Summary of the Audio measurements of the test runs with the frequency peaks in the chatter, squeal, and high frequency squeal regions; the blue rows are wet runs and the yellow rows are the dry runs

7.1.3. Symmetric loading

To counter the close range eigen frequencies of the brake pads and the rotor as observed via finite element simulations, the mass of the rotor was increased symmetrically to change its natural frequencies. A nut, a bolt and 10 washers formed one body weighing 9 grams. Seven such bodies were added on the seven ribs of the rotor as shown in the Figure 7.4. These seven bodies increased the overall mass of the rotor by 30% from 215 grams to 278 grams. Symmetric loading was very effective in not only reducing the brake noise magnitude but also in bringing the frequency range of the brake noise down. Figure 7.2 displays the brake noise audio results for the symmetric loading in comparison with the reference runs and other countermeasures. Table 7.4 captures the difference in the magnitude and frequency of the brake noise between the reference run and the symmetrically loaded run. A drop of 12 decibels in chatter magnitude, 7 decibels in squeal magnitude, and 8.6 decibels in high-frequency squeal magnitude was achieved. An increase in rotor mass by 63 grams brought down the squeal and high-frequency squeal frequencies of vibration by an average 24.2 Hz and 33.8 Hz respectively.

Brake noise	Reference		Sym. loaded		% Magnitude reduction	Decibel change
	Frequency (Hz) (average)	Magnitude (voltage) (average)	Frequency (Hz) (average)	Magnitude (voltage) (average)		
Chatter	580.8	4833.9	568.4	1210.3	75	12
Squeal	1162.6	6155.5	1138.4	2726.7	55.7	7
High freq. squeal	1740.8	2124.9	1707	788.8	63	8.6

Table 7.4: Comparison of the brake noise magnitude and frequency of the symmetrical loading of the rotor with the reference run

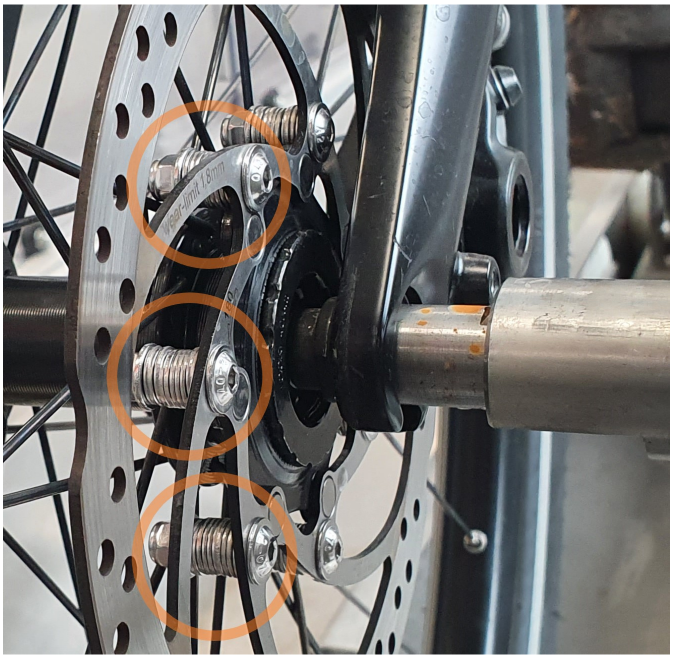

Figure 7.4: Nuts, bolts, and washers added to all the ribs of the rotor to increase its overall mass and decrease its natural frequency

7.1.4. Asymmetric loading

To counter the flutter instability caused due to the convergence of doublet modes in the structure, asymmetries were introduced by means of adding masses of 9 grams just like in the symmetric loading but not to all the ribs of the rotor. Four such bodies of mass were added on four consecutive ribs of the rotor, thereby causing one half of the rotor to be heavier than the other. Figure 7.5 shows the asymmetric loading on the rotor. The overall mass of the rotor was increased by 17%. The results of the audio scans are displayed in Table 7.3. Of all the countermeasures tested in the present study,

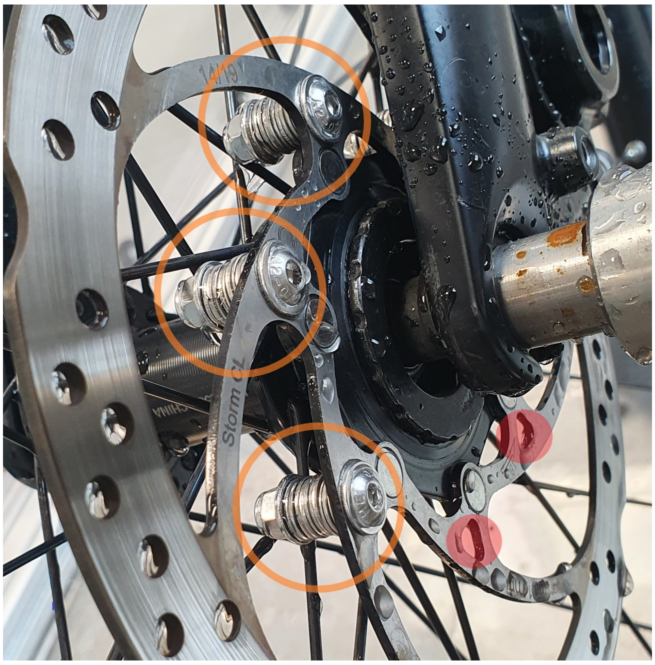

Figure 7.5: Nuts, bolts, and washers added to only four ribs of the rotor to cause an asymmetric distribution of mass; orange circles highlighting the additional weights and red dots highlighting the absence of the masses

asymmetric loading performed the best in reducing the magnitude of the brake noise. Asymmetric loading was able to damp the high-frequency squeal completely as shown in Figure 7.2 where no third peak (in black) for the asymmetric loading is seen. A slight reduction in the peak frequencies was also expected for this type of loading because of an increase in the overall mass of the rotor. A comparison of the asymmetrical loading run with the reference run is shown in Table 7.5.

Brake noise	Reference		Asymmetrically loaded		% Magnitude reduction	Decibel change
	Frequency (Hz) (average)	Magnitude (voltage) (average)	Frequency (Hz) (average)	Magnitude (voltage) (average)		
Chatter	580.8	4833.9	574.4	1353.8	72	11
Squeal	1162.6	6155.5	1150.5	1669.3	73	11.32
High freq. squeal	1740.8	2124.9	-	-	99.9	66

Table 7.5: Comparison of the brake noise magnitude and frequency of the asymmetrical loading of the rotor with the reference run

7.2. Finite Element Analysis

The finite element model developed in this project is limited only to structural analysis and ignores the thermal gradients in the model. As mentioned above, the slotted brake pad limits the brake noise by improving the heat conduction at the sliding interface; the finite element model fails to capture this. In theory, the slots in the brake pads should lower the natural frequency of the brake pad and the system but the experiments did not capture any difference in the brake noise frequency between the slotted pad runs and the reference runs (see Table 7.3). Therefore, the slots in the brake pads were not simulated in ANSYS for this project.

To simulate the symmetric and asymmetric loading in ANSYS, a simplification was made where the rotor and the added weights were considered as one single body instead of considering rotor and the 10 washers as 11 bodies. The nuts, bolts, and the washers were modeled as cylinders on the rotor. As mentioned before, Magura STORM CL rotor was used in the experimental countermeasure study. For ANSYS simulations, Magura rotor was not modeled and Shimano rotor that was modeled for the earlier simulations in chapter 5 was modified. Figure 7.6 shows the finite element rotor models for symmetric and asymmetric loading. The entire simulation process was repeated as discussed in chapter 5 and chapter 6 with just the rotor shape changed in the model. The results from chapter 6 formed the reference state for the finite element countermeasure studies. The location and the mass of the cylinders were not the same as the nuts and bolts from the experiments. The idea here was not to reproduce the experiments on ANSYS 1:1 but to capture the changes in the eigen frequencies and the mode shapes that could explain the suppression of brake noise during the experiments.

The added cylinders were successful in bringing the eigen frequencies of the system down just like the added masses in the experiments. Table 7.6 shows the eigen frequencies of the system in its base state, symmetrically loaded state, and asymmetrically loaded state. Even though more eigen frequencies were found in the loaded states, there were lesser eigen frequencies in the unstable regions of chatter, squeal, and high-frequency squeal. There were no noticeable changes in the amplitude of vibrations observed in the three FE models of no loading, symmetric loading, and asymmetric loading.

7.2.1. Asymmetric loading

Asymmetrical loading had no eigen frequencies in the region of high-frequency squeal that resembled the mode shape from the experiments and the base state simulations. Some of the mode shapes for the asymmetric loading were not symmetric and half of the assembly vibrated more than the other, which was to be expected because of the asymmetric distribution of mass on the brake assembly. This change in mode shapes in the asymmetric loading was observed more in the squealing regions than in the chatter, which explains the absence of frequency peak in the high-frequency region in the brake noise audio scans (see Figure 7.2). Figure 7.7 summarizes all the eigen frequencies along with the simplified mode shape of the asymmetric and symmetric loading cases.

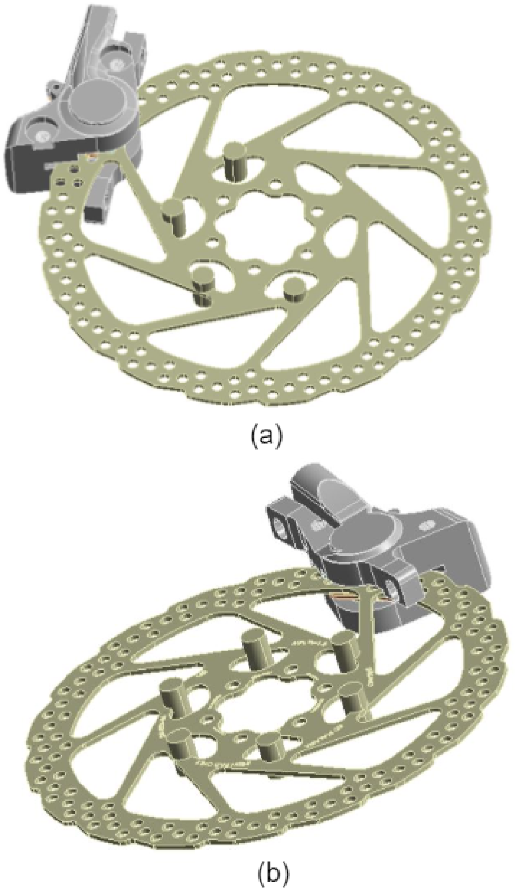

Figure 7.6: Finite element model for the (a) Asymmetric loading of the rotor (b) Symmetric loading of the rotor

Reference		Symmetrical loading		Asymmetrical loading		Description
Mode	Frequency (Hz)	Mode	Frequency (Hz)	Mode	Frequency (Hz)	
1	543.75	1	533.58	1	532.31	Mode shape: (2,1)
		2	700.93	2	700.42	In-plane mode
2	732.12	3	719.54	3	718.55	Mode shape: (2,1)
3	943.5	4	935.95	4	935.01	Mode shape: (3,1)
4	1072					In-plane mode
5	1167	5	1157.3	5	1156.4	Mode shape: (3,1)
		6	1226.6	6	1226.4	In-plane mode
		7	1403.8	7	1403.9	In-plane mode
6	1510.1	8	1503.7	8	1503.4	Mode shape: (4,1)
7	1811.3	9	1646			Mode shape: (0,2)
		10	1735.4			Mode shape: (1,2)
8	1827.5	11	1818.6			Mode shape: (4,1)
				9	1688.8	Asymmetric
				10	1802.9	Asymmetric
9	1864.2					In-plane mode

Table 7.6: Eigen frequencies of the brake assembly between 0-2000 Hz with chatter doublet highlighted in red, squeal doublet in blue, and high frequency squeal doublet in green. The frequencies of the doublet have decreased under the loaded cases and in some cases the doublet is missing

7.2.2. Symmetric loading

The natural frequencies extracted from the symmetrical and asymmetrical loaded finite element models were very similar, which was not the case in the experiments. This can be attributed to the placement and the mass difference between the cylinders and the nuts and bolts. The symmetric loading finite element model had three new modes of vibration appear but none of the new modes fell in the chatter and squeal regions. Symmetric loading of the rotor managed to decrease its natural frequencies, which ultimately lowers the lock-in frequencies of the rotor and the brake pad (see Table 7.6). This observation is in accordance with the results of the experiments, where a decrease in the natural frequencies was also captured.

7.3. Summary

In order to counter the modal lock-in present in the assembly, the mass of the rotor was increased symmetrically and asymmetrically and tested on the brake test machine by taking brake noise audio measurements. Both kinds of loadings were successful in reducing the brake noise magnitude by over 50%. Symmetric loading also managed to bring the frequencies of vibration down. Asymmetric loading performed the best in reducing the brake noise magnitude, it completely suppressed the third frequency peak.

Another countermeasure that was tested was the parallel slot in the brake pad. Slots and holes are adopted by automotive brake manufacturers to improve heat conduction but not many bike manufacturers use slots in their pads. Just like the loadings, slotted brake pads were also tested on the brake test machine by measuring the brake noise. Slots in brake pads also decreased the brake noise magnitude but barely affected the frequencies of vibrations. Overall, both the loadings performed better than the slot.

Simplified finite element model of the modified rotors was also designed and analyzed. The finite element model showed a decrease in vibration frequencies as expected but what was not foreseen was an increase in the number of eigen frequencies in the system. Overall there was a decrease in the number of eigen frequencies in the unstable regions of chatter, squeal, and high-frequency squeal. The asymmetric model had completely different and asymmetric mode shapes. There was no symmetric mode in the high-frequency squeal region, which correlated well with the experimental results. The finite element model did not capture any changes in the amplitude of vibrations of the brake system in the symmetrically loaded, asymmetrically loaded, and the reference state.

Symmetric loading				Asymmetric loading			
Mode	**Frequency**	**Mode Shape Interpretation**	**Mode shape**	**Mode**	**Frequency**	**Mode Shape Interpretation**	**Mode shape**
1	533.6 Hz	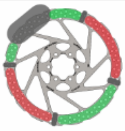	(2,1)	1	532.3 Hz	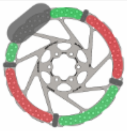	(2,1)
2	700.9 Hz	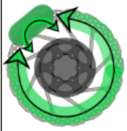	In-plane	2	700.4 Hz	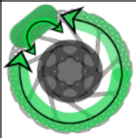	In-plane
3	719.5 Hz	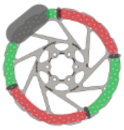	(2,1)	3	718.5 Hz	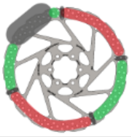	(2,1)
4	935.9 Hz	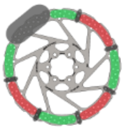	(3,1)	4	935 Hz	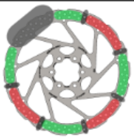	(3,1)
5	1157.3 Hz	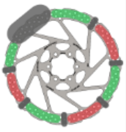	(3,1)	5	1156.4 Hz	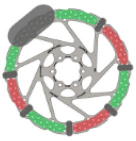	(3,1)
6	1226.6 Hz	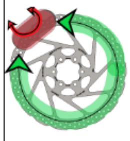	In-plane	6	1226.4 Hz	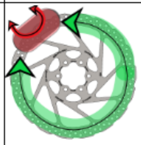	In-plane
7	1403.8 Hz	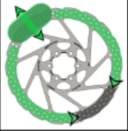	In-plane	7	1403.9 Hz	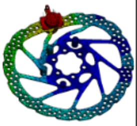	In-plane
8	1503.7 Hz	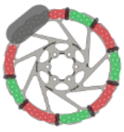	(4,1)	8	1503.4 Hz	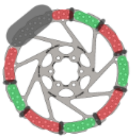	(4,1)
9	1646 Hz	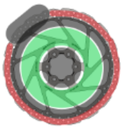	(0,2)	9	1688.8 Hz	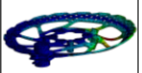	Asym
10	1735.4 Hz	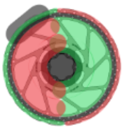	(1,2)	10	1802.9 Hz	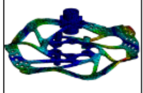	Asym
11	1818.6 Hz	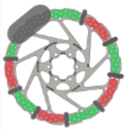	(4,1)				

Figure 7.7: Summary of the eigen frequencies and the mode shapes of the symmetrically loaded and asymmetrically loaded cases; gray areas are the nodes and the green and red areas are the positive and negative displacements; the arrows are for the in-plane modes that show the direction the body is vibrating in

8

Conclusion and Future Recommendations

The overall aim of this project was to focus on the sliding interface of the brake pad and the rotor to gain insight into the vibration characteristics of the brake assembly and devise ways to reduce the brake noise. The test bench setup consisting of the brake test machine designed by Schmidt Engineering GmbH was used to run the bicycle in the laboratory settings. Brake noise audio scans via a microphone placed close to the pad-rotor interface were taken. PSV-400 vibrometer was used to perform an experimental modal analysis of the brake assembly.

Stick-slip, which is one of the mechanisms that give rise to the self-excited friction-induced vibrations, was observed during the experimental investigations. Brake noise audio scans revealed that brake noise that we hear is basically the three peak frequencies of the noise of 580 Hz, 1160 Hz, and 1740 Hz classified as chatter, squeal, and high-frequency squeal respectively. The squeal and high-frequency squeal are the most annoying to the human ear because of human hearing being the most sensitive in the regions of 1-4 kHz. On the decibel scale, the brake noise was recorded at 97±5 decibels. The dynamics of different parts of the bike under chatter and squeal regions were captured. It was found out that the entire bike vibrated at the above-mentioned three frequencies during a brake noise event. The bike parts vibrated at a velocity of as high as 1.5 mm/s. The results clearly showed that the vibrations originated from the pad-rotor interface and traveled to the surrounding bike components. Brake pads, rotor, and brake caliper was modeled in the Solidworks keeping in mind the simplicity and reproducibility of the model for future simulations. Pre-stressed modal analysis was carried out on the brake assembly and the results of the simulations were compared with the experimental data and the finite element model was successfully validated. The finite element model was successfully able to predict the mode shapes and eigen frequencies of the real-life brake system. The frequencies from the simulations and the experimental investigation had a maximum difference of only 45 Hz and no difference in the mode shapes. In addition to this, the finite element model could also predict the presence of in-plane vibration modes in a squeal, which the laser Doppler vibrometer was not able to generate. Doublet mode that lead to flutter instability in the system and intermediate mode lock-in were identified during the finite element simulations.

Based on the observations from the experiments and simulations, three countermeasures (A parallel slot in the brake pad, a symmetrically loaded rotor, and an asymmetrically loaded rotor) were tested both experimentally and analytically. Asymmetric loading of the rotor was devised to tackle the problem of doublet modes. It completely suppressed the high-frequency squeal, and decreased the chatter magnitude by 11 decibels, and the squeal magnitude by 11.32 decibels. The finite element simulations of the asymmetric model show a change in the modes of vibrations of the brake assembly. There existed no symmetrical modes in the high-frequency squeal region and the overall frequency of the modes also decreased. Similar to asymmetric loading, symmetric loading of the rotor was also successful in lowering the magnitude and frequencies of the modes of vibrations. Symmetric loading was devised to tackle the intermediate mode lock-in between the pads and the rotor. The FE simulations showed a decrease in the eigen frequencies of the rotor in its loaded state. A decrease of 12 decibels in chatter magnitude, 7 decibels in squeal magnitude, 8.6 decibels in the high-frequency squeal magnitude was observed. The third countermeasure that was tested was to improve the heat balance and allow for better conduction. A parallel slot was made into the frictional lining and tested for the results. It managed to reduce the chatter, squeal, and high-frequency squeal magnitude by 4.2 decibels, 1.73 decibels, and 7.35 decibels. Of the three countermeasures that were tested, asymmetric loading worked the best in reducing the magnitude and frequency of the vibrating structure.

8.1. Future Work

Despite a century of developing disc brake systems, disc brake noise is far from being completely understood and the problem still remains largely unresolved. The work carried out during the course of this project was unique in its implementation and provided some key observations for future work. The experimental investigation using the laser Doppler vibrometer and the finite element simulations provided an increased understanding of the mechanism for instability generation. However, the finite element simulations were performed using a caliper model that had some noticeable geometry differences to the actual caliper part used in the experimental study. Thus, accurately modeling the caliper part and enabling the effect of support system would provide valuable information towards the instability generation mechanisms and make the present approach more complete.

The present work did not take into account the effect of damping. Damping is one of the key factors that can influence the stability of any system. It is therefore recommended to consider damping in the future finite element models to perceive its effects on the system instability.

The present finite element model assumes a constant friction coefficient at the sliding interface but in reality, friction mechanisms like stick-slip causes a variation in the friction coefficient while the surfaces slide. Future studies can look into ways to introduce the variable friction coefficient in the model and study its effects on the dynamics of the brake system.

The present finite element model also considers a smooth surface for the friction lining, it is recommended that the information regarding the friction material is extracted from the real surface of the brake pads and incorporated in the model.

The finite element model's center of pressure was also unresponsive to the change in hydraulic pressure. In practical situations the contact area varies with different hydraulic pressures, which affects the center of pressure and the brake noise propensity. It is recommended to perform finite element analysis to understand the main reason for this.

For the countermeasure studies performed in this project, optimization techniques can be used to find the optimal placement and the quantity of the additional mass on the rotor. Instead of adding additional mass to introduce asymmetries in the rotor, geometric asymmetries by changing the rotor design needs to be studied. The shapes and position of the slots and holes on the brake pad can also be further optimized by introducing the thermal analysis and linking it to the structural analysis on ANSYS. The effects of the additional masses on the rotor and the slots on the brake pads were studied keeping in mind the brake noise problem, however, the effects of these modification on the braking performance was not studied. The bicycle manufacturers can study the effects of such modifications on their bikes.

8.2. Final Remarks

The overall aim of this project was to gain insight into the vibration characteristics of the brake assembly and develop an understanding of the self-excited friction-induced instabilities in the bicycles. This has been achieved by means of experimentation and finite element simulations. A number of simplifications were made during the testing and simulations due to the time, financial, and computational power constraints. However, the findings presented in this thesis have still demonstrated a significant contribution towards an understanding of the bicycle disc brake noise and its characteristics.

A

Matlab Script

The Matlab script that was used to convert the audio scan data into frequency domain is shared below:

```
%loading the file
%sound(y,Fs) plays the sound
y,Fs = audioread(’St1.m4a’)

%sound(y,Fs);

%PART A


%number of samples
n=length(y)
%time=samples/(samples/seconds)=seconds
t = (1:n)/Fs;
figure
plot(t,y)
title(’Time Vs Amplitude’)
xlabel(’Time(sec)’)
ylabel(’Amplitude’)

%PART B

%using fft to convert into frequency domain
Y = fft(y);
%transforming time into frequency
freq = (1:n)/n*Fs;
figure
plot(freq(1:n/2),abs(Y(1:n/2)))
title(’Frequency Vs Amplitude’)
xlabel(’Frequency’)
ylabel(’Amplitude’)
```

B

Audio Amplitude Vs. Frequency Plots

Amplitude vs. Frequency plots for the test runs discussed in chapter 4 are presented here. The first five plots are for the wet weather runs and the next five plots are for the dry weather runs.

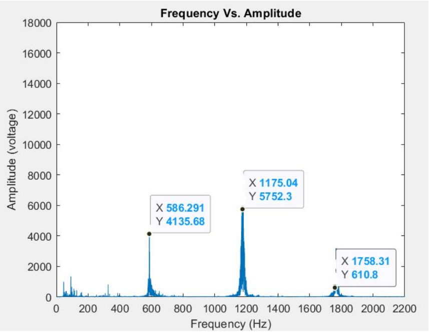

Figure B.1: Amplitude Vs. Frequency plot of the test run 1 revealing three peak frequencies; first peak is the chatter range, second peak is in the squeal range, and the third peak is in the high-frequency squeal range

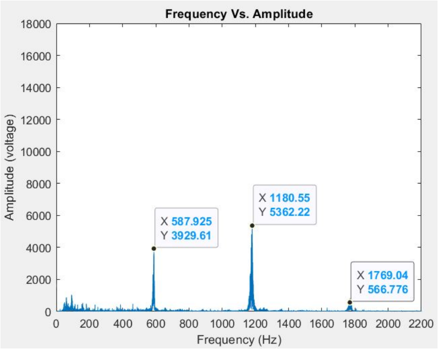

Figure B.2: Amplitude Vs. Frequency plot of the test run 2 revealing three peak frequencies; first peak is the chatter range, second peak is in the squeal range, and the third peak is in the high-frequency squeal range

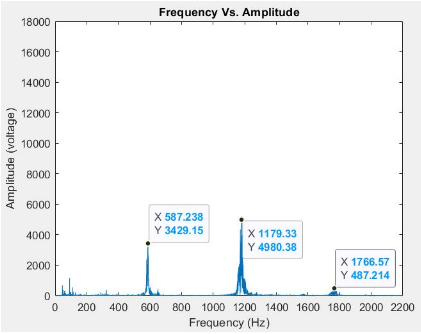

Figure B.3: Amplitude Vs. Frequency plot of the test run 3 revealing three peak frequencies; first peak is the chatter range, second peak is in the squeal range, and the third peak is in the high-frequency squeal range

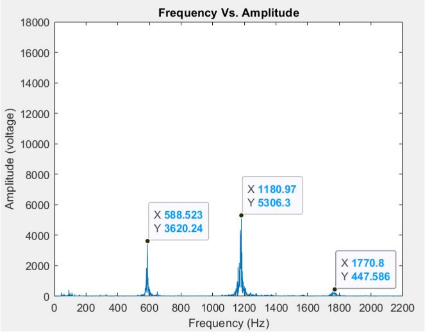

Figure B.4: Amplitude Vs. Frequency plot of the test run 4 revealing three peak frequencies; first peak is the chatter range, second peak is in the squeal range, and the third peak is in the high-frequency squeal range

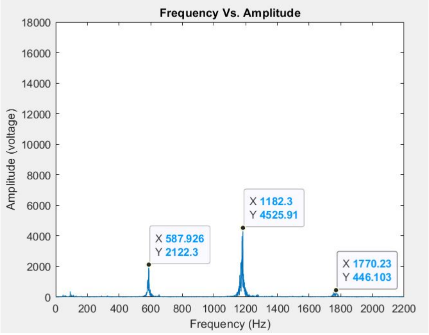

Figure B.5: Amplitude Vs. Frequency plot of the test run 5 revealing three peak frequencies; first peak is the chatter range, second peak is in the squeal range, and the third peak is in the high-frequency squeal range

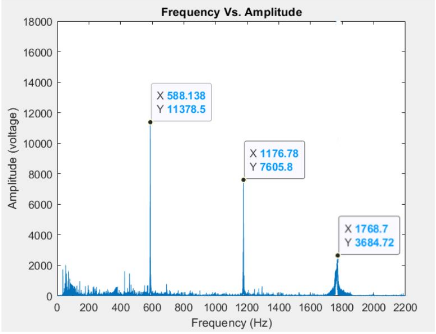

Figure B.6: Amplitude Vs. Frequency plot of the test run 6 revealing three peak frequencies; first peak is the chatter range, second peak is in the squeal range, and the third peak is in the high-frequency squeal range

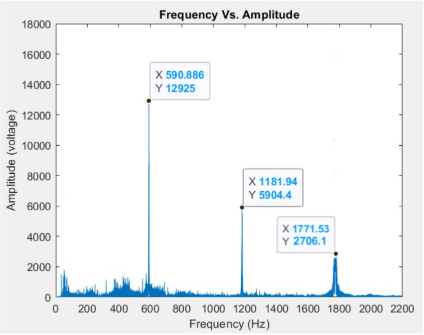

Figure B.7: Amplitude Vs. Frequency plot of the test run 7 revealing three peak frequencies; first peak is the chatter range, second peak is in the squeal range, and the third peak is in the high-frequency squeal range

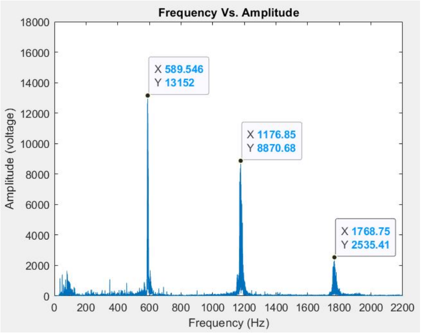

Figure B.8: Amplitude Vs. Frequency plot of the test run 8 revealing three peak frequencies; first peak is the chatter range, second peak is in the squeal range, and the third peak is in the high-frequency squeal range

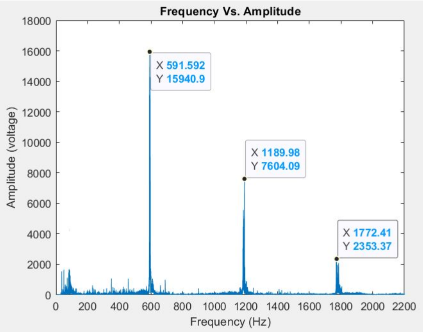

Figure B.9: Amplitude Vs. Frequency plot of the test run 9 revealing three peak frequencies; first peak is the chatter range, second peak is in the squeal range, and the third peak is in the high-frequency squeal range

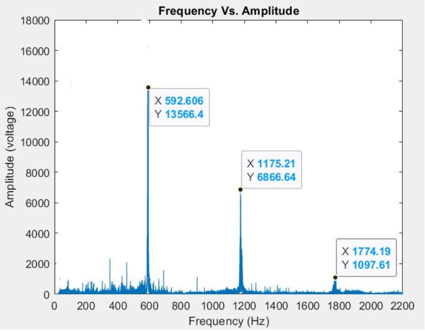

Figure B.10: Amplitude Vs. Frequency plot of the test run 10 revealing three peak frequencies; first peak is the chatter range, second peak is in the squeal range, and the third peak is in the high-frequency squeal range

C

Vibrometer Magnitude Vs. Frequency Plots

Amplitude vs. Frequency plots for the test runs as captured by the laser Doppler vibrometer discussed are presented here. The first ten plots are of the brake noise events in which the first five plots are for the wet weather runs and the next five plots are for the dry weather runs. The last five plots are for the no noise events which only happens under dry conditions.

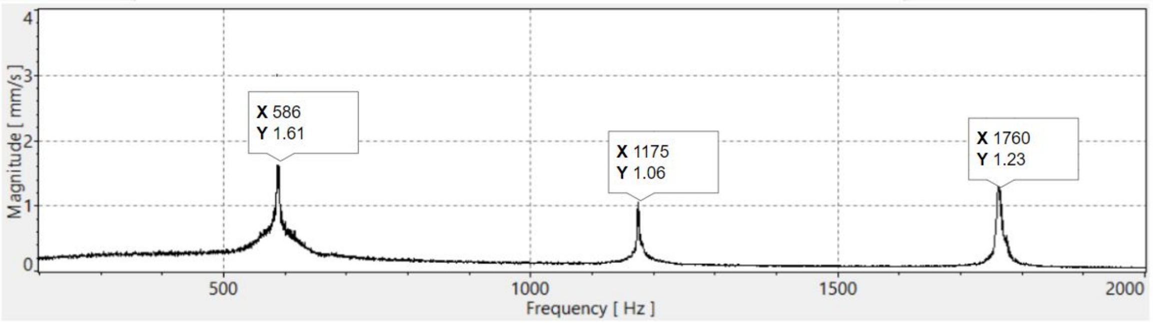

Figure C.1: Magnitude Vs. Frequency plot of the test run 1 revealing three peak frequencies for the vibrating rotor under brake noise event

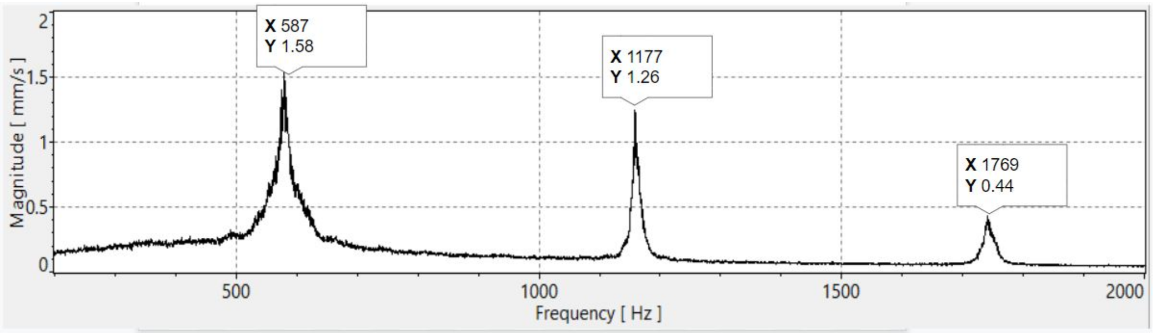

Figure C.2: Magnitude Vs. Frequency plot of the test run 2 revealing three peak frequencies for the vibrating rotor under brake noise event

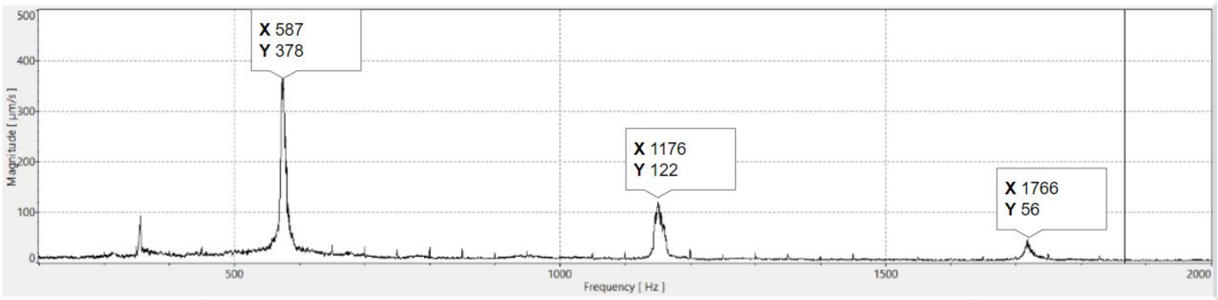

Figure C.3: Magnitude Vs. Frequency plot of the test run 3 revealing three peak frequencies for the vibrating front fork under brake noise event

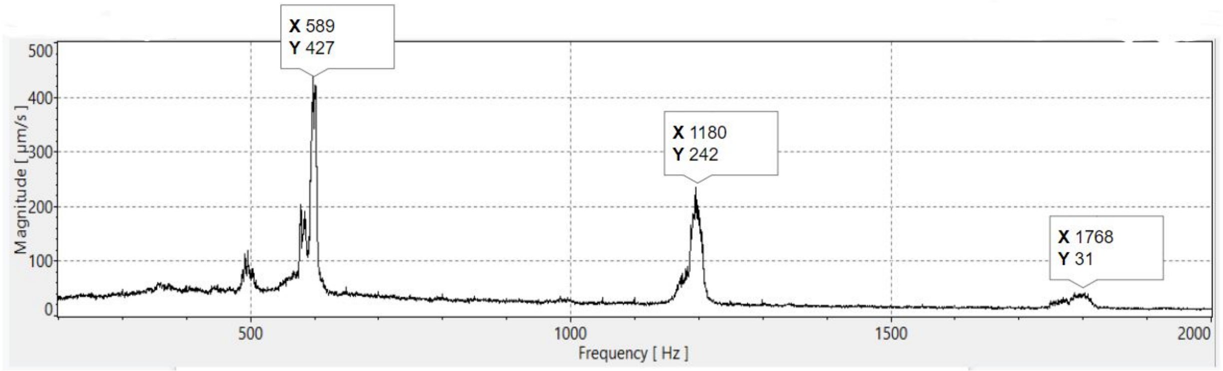

Figure C.4: Magnitude Vs. Frequency plot of the test run 4 revealing three peak frequencies for the vibrating front fork under brake noise event

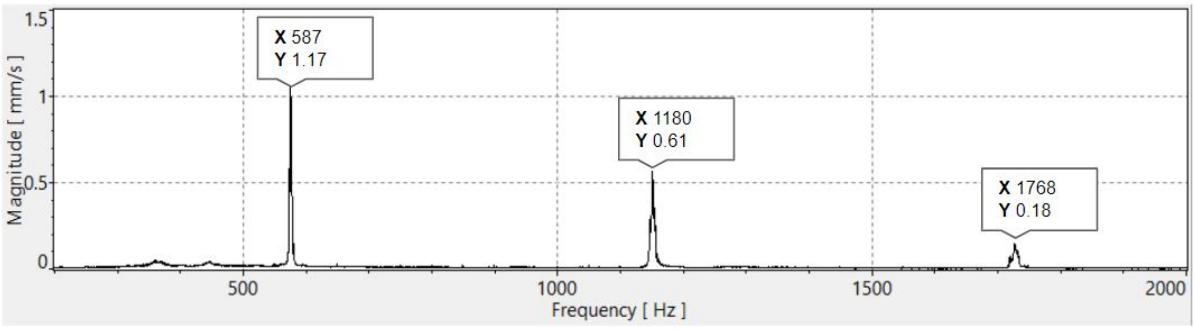

Figure C.5: Magnitude Vs. Frequency plot of the test run 5 revealing three peak frequencies for the vibrating caliper under brake noise event

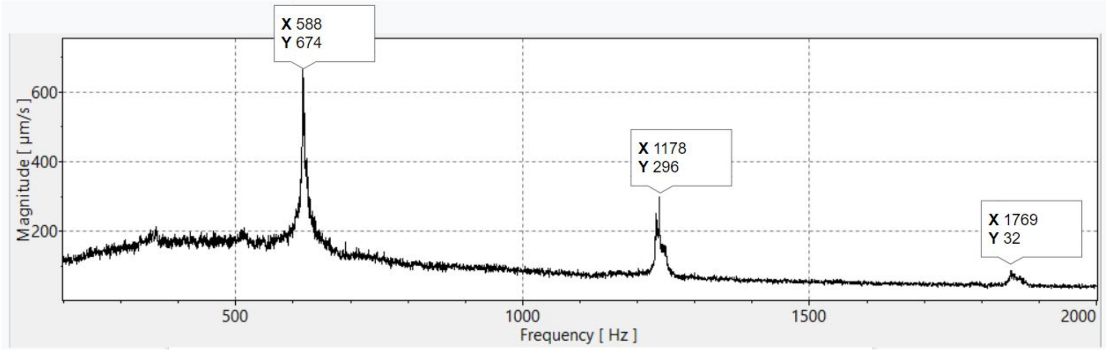

Figure C.6: Magnitude Vs. Frequency plot of the test run 6 revealing three peak frequencies for the vibrating rotor under brake noise event

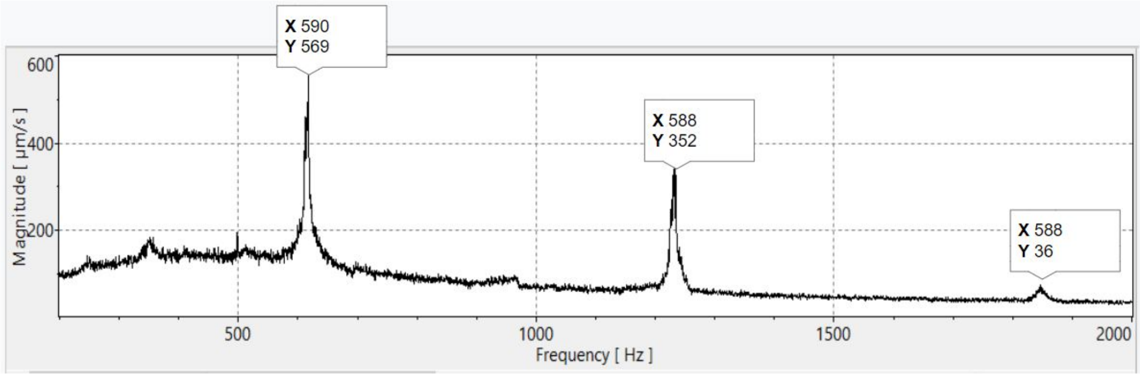

Figure C.7: Magnitude Vs. Frequency plot of the test run 7 revealing three peak frequencies for the vibrating rotor under brake noise event

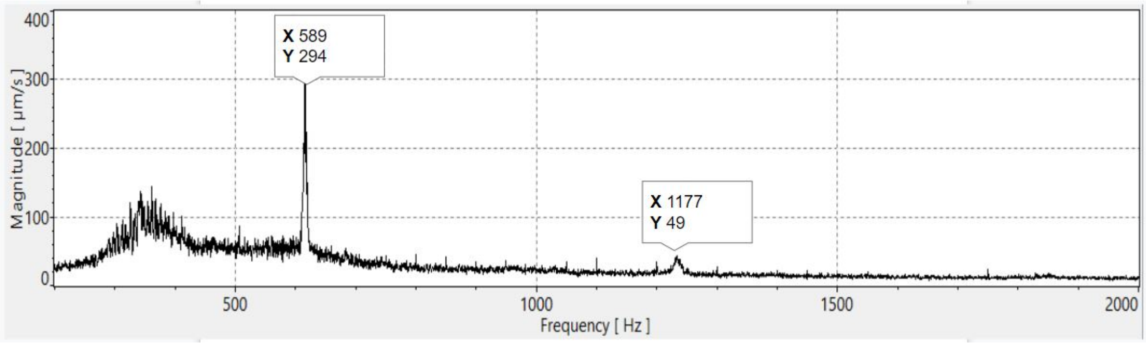

Figure C.8: Magnitude Vs. Frequency plot of the test run 8 revealing three peak frequencies for the vibrating front fork under brake noise event

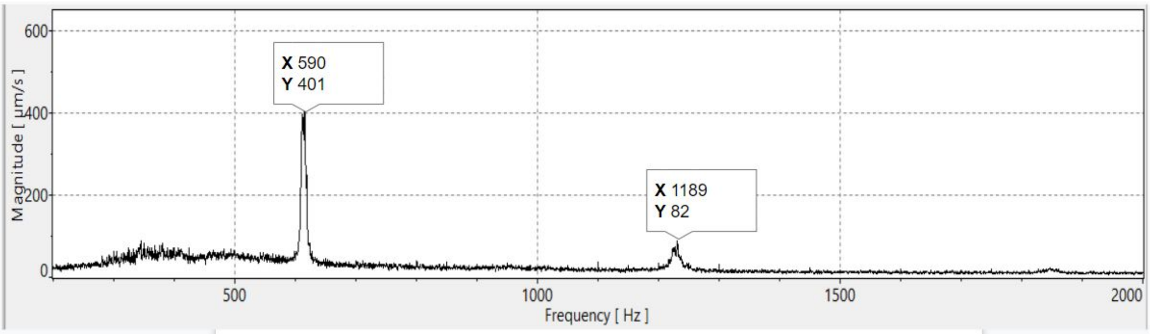

Figure C.9: Magnitude Vs. Frequency plot of the test run 9 revealing three peak frequencies for the vibrating front fork under brake noise event

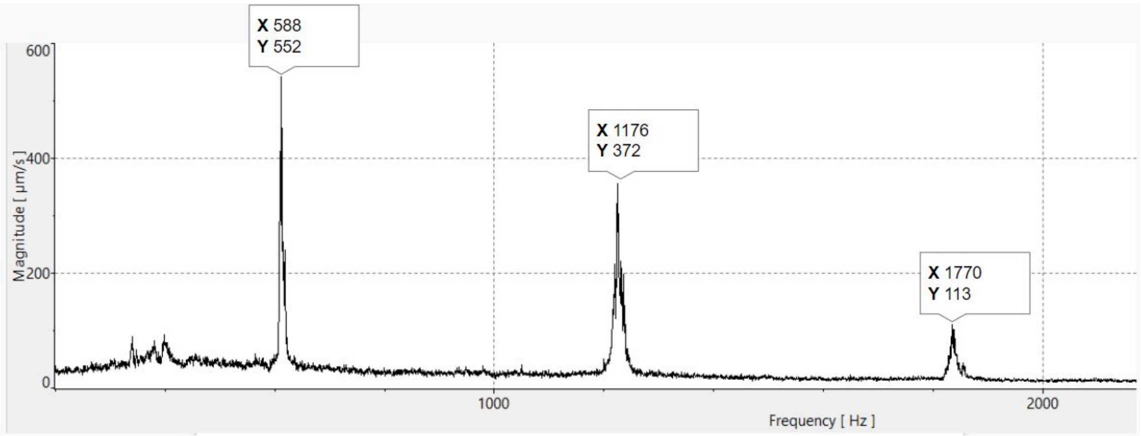

Figure C.10: Magnitude Vs. Frequency plot of the test run 10 revealing three peak frequencies for the vibrating caliper under brake noise event

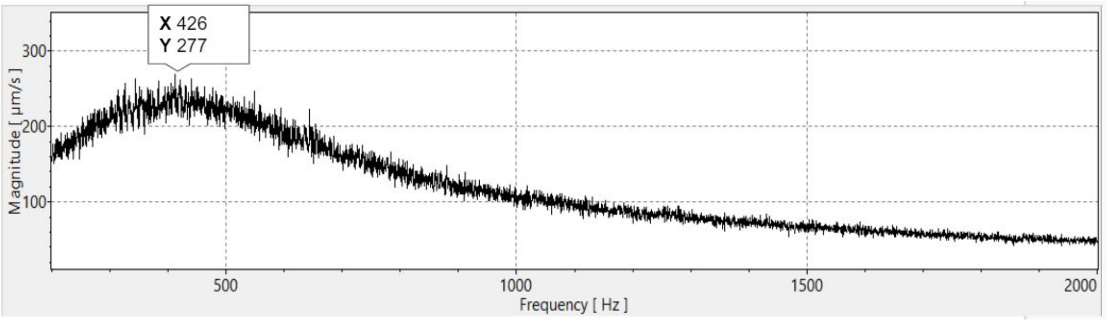

Figure C.11: Magnitude Vs. Frequency plot of the test run 11 revealing three peak frequencies for the vibrating rotor under no noise event

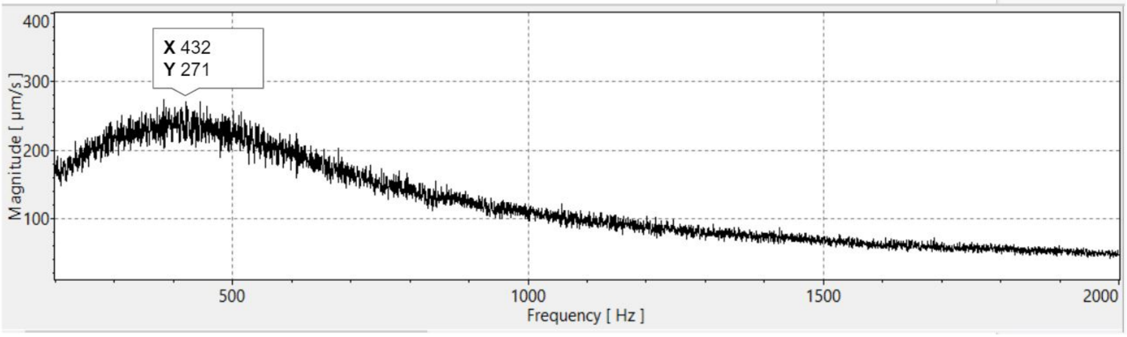

Figure C.12: Magnitude Vs. Frequency plot of the test run 12 revealing three peak frequencies for the vibrating rotor under no noise event

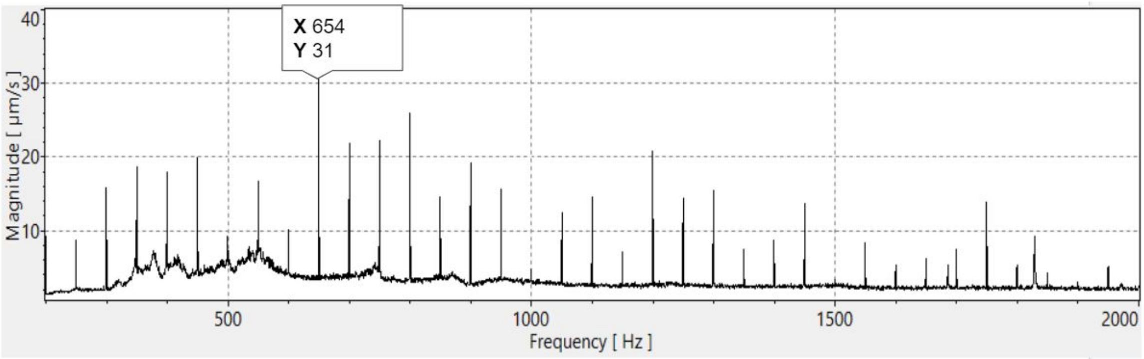

Figure C.13: Magnitude Vs. Frequency plot of the test run 13 revealing three peak frequencies for the vibrating front fork under no noise event

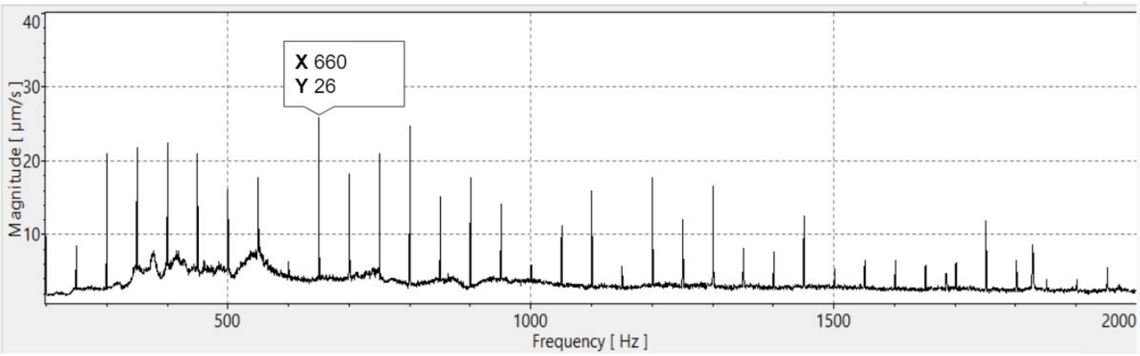

Figure C.14: Magnitude Vs. Frequency plot of the test run 14 revealing three peak frequencies for the vibrating front fork under no noise event

D

Derivation of stress matrix in the stiffness matrix

Delving deeper into the theory of finite element analysis to figure out where this stress matrix comes from in the stiffness matrix. When a system is acted upon by external loads, stresses are formed. These stresses lead to deformations and the deformations result in displacements. There are three governing equations while performing the prestressed modal analysis:

Continuity equation

$$Displacements \longrightarrow Deformations$$

Constitutive equation

$$Deformations \longrightarrow Stresses$$

Equilibrium equation

$$Stresses \longrightarrow ExternalLoads$$

Let us consider a triangular piece of material or a single element of an FEA model as shown in the Figure D.1. The element has three nodes on each side and at each node kinematic degree of freedom is introduced (displacements). The element shares its nodes with its neighboring elements and the displacement fields are also shared by all the neighboring elements as shown in Figure D.2. The blue cubes inside the elements are the integration points where the displacements and the deformations of the elements are calculated and the shape functions/interpolation functions are used to interpolate the kinematics of the nodes at these integration points. The integration points are used to calculate the strain energy and these are also the places where the history of the material is tracked. For example, plasticity is a material property that is history-dependent. For simplicity purposes, it is smart to keep a

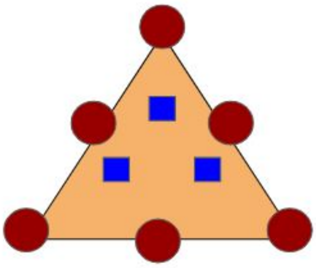

Figure D.1: Triangular element of the FEA model with nodes in red and integration points in blue

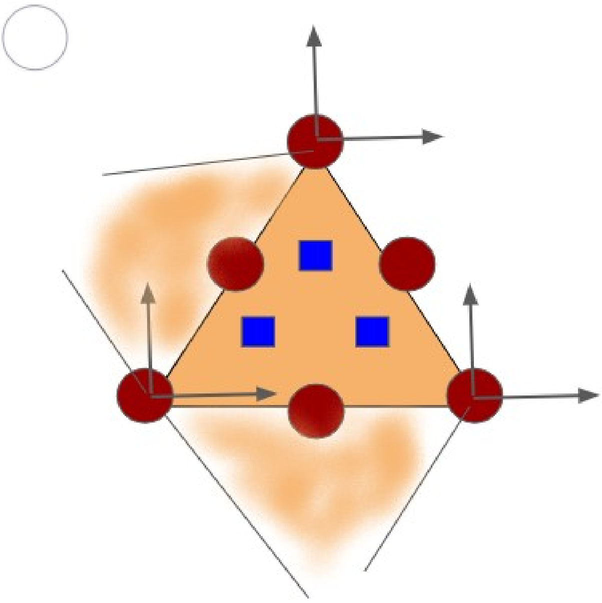

Figure D.2: Degrees of freedom of the nodes and the neighboring elements of the element in a mesh

track of such material history only for a select few points instead of keeping track at every point.
To summarise, a real structure is modeled using finite elements for which all the properties are known and these tiny elements are connected to each other via nodal points. These connections ensure that continuity is satisfied over the boundaries of all the finite elements. If the displacements at the nodes are known, the deformations inside the element (usually at the integration points) can be calculated. For the integration points, generalized deformations, ξ are calculated. The deformations are a function of degrees of freedom, d for the element k.

$$\xi^k = \xi^k[d^k] \tag{D.1}$$

Consider a 2D truss element with displacements at nodes as shown in Figure D.3. To calculate the generalized deformations on the truss element at any arbitrary point, $\bar{x}$ between the two nodes, a shape function η is used, which is given as

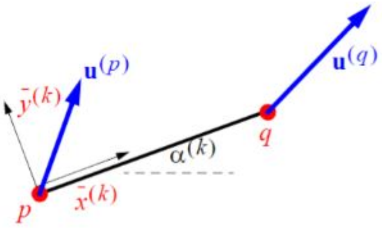

Figure D.3: 2D truss element with displacements at the nodes

$$\eta = \frac{\overline{x}}{L} \tag{D.2}$$

The shape functions are coupled to the definition of the element. Every element has a different shape function and depending on the convenience and suitability, a certain type of element is chosen. The FEA software generates a unique shape function for every different element. Shape functions are used to define the relationship between the degrees of freedom and the generalized deformations. The deformations at an arbitrary point, $\bar{x}$ are as follows

$$\begin{bmatrix} u_{\bar{x}} \\ u_{\bar{y}} \end{bmatrix} = \begin{bmatrix} (1-\eta) & 0 & \eta & 0 \\ 0 & (1-\eta) & 0 & \eta \end{bmatrix} \begin{bmatrix} u_{\bar{x}}^{p} \\ u_{\bar{y}}^{p} \\ u_{\bar{x}}^{q} \\ u_{\bar{y}}^{q} \end{bmatrix} \tag{D.3}$$

The continuity equation can be written as

$$\xi^k = L^k[E_{\overline{xx}}] = L^k\left[\frac{du_{\bar{x}}}{d\bar{x}} + \frac{1}{2}\left(\left(\frac{du_{\bar{x}}}{d\bar{x}}\right)^2 + \left(\frac{du_{\bar{y}}}{d\bar{x}}\right)^2\right)\right] \tag{D.4}$$

where $E_{\overline{xx}}$ is the Green-Lagrange strain tensor and L^k is the length of the element k.
Substituting the shape function and the strain tensor in the continuity equation, the generalized deformations, $\xi^k[d^k]$ are

$$\xi^k[d^k] = \begin{bmatrix} -1 & 0 & 1 & 0 \end{bmatrix} \bar{d}^k + \frac{1}{2L^k}(\bar{d}^k)^T \begin{bmatrix} 1 & 0 & -1 & 0 \\ 0 & 1 & 0 & -1 \\ -1 & 0 & 1 & 0 \\ 0 & -1 & 0 & 1 \end{bmatrix} \bar{d}^k \tag{D.5}$$

where the degrees of freedom, d^k are

$$(\bar{d}^k)^T = \begin{bmatrix} u_{\bar{x}}^{p} & u_{\bar{y}}^{p} & u_{\bar{x}}^{q} & u_{\bar{y}}^{q} \end{bmatrix} \tag{D.6}$$

The generalized deformations, ξ^k follow a linear and non-linear displacement field as seen in the equation 12. The non-linear displacement field becomes essential once the deformations and rotations become finite or when there is an influence of stress on the stiffness.
Now, slight variations, δd^k are brought to the degrees of freedom to evaluate the effects of the virtual displacements, $\delta\xi^k$ on the generalized deformations.

$$d^k \longrightarrow d^k + \delta d^k \tag{D.7}$$

$$\xi^k \longrightarrow \xi^k + \delta\xi^k \tag{D.8}$$

$$\delta\xi_i^k = \sum_j \frac{\partial \xi_i^k}{\partial d_j^k}\delta d_j^k \tag{D.9}$$

the range of j for the truss elements is $j = 1...4$
Equation (D.9) can be rewritten as

$$\delta\xi^k = D^k[d^k]\delta d^k \tag{D.10}$$

where D^k is

$$D_{ij}^k = \frac{\partial \xi_i^k}{\partial d_j^k} \tag{D.11}$$

the D matrix establishes a relationship between the virtual displacements and the corresponding virtual changes in the deformations. The current configuration of an element influences the D matrix, as it can be seen from the equations (D.10) & (D.11) that it is a function of degrees of freedom, d. So if the element is deformed, rotated, or translated, it will have an effect on the D matrix.
Now looking at the principle of virtual work, δW_i for the internal part. The internal virtual work can be calculated by the inner dot product of the virtual displacements, $\delta\xi^k$ and the corresponding generalized stresses, ζ^k.

$$\delta W_i = \sum \zeta^k \cdot \delta\xi^k \tag{D.12}$$

Substituting (D.10) in (D.12)

$$\delta W_i = \sum \zeta^k \cdot D^k[d^k]\delta d^k \tag{D.13}$$

In a truss element, the generalized deformations are

$$\xi^k = L \cdot E_{\overline{xx}} \tag{D.14}$$

that means the corresponding generalized stress for the component is

$$\zeta^k = A \cdot S_{\overline{xx}} \tag{D.15}$$

where L and A are the length and the cross section of the element. ξ^k is nothing but a change in the length, ΔL of the element and ζ^k is the force, N in the element. Therefore, these two terms can be multiplied to derive the energy terms for the entire system. The internal virtual work for the system of elements is

$$\delta W_i = \zeta \cdot D[d]\delta d \tag{D.16}$$

The virtual work by the external loads, δW_u is

$$\delta W_u = f \cdot \delta d \tag{D.17}$$

The external virtual work is the dot product of the degrees of freedom and the nodal loads, f.
For equilibrium

$$\delta W_u = \delta W_i \tag{D.18}$$

Substituting (D.16) and (D.17) in (D.18)

$$f = D^T \cdot \zeta \tag{D.19}$$

The degrees of freedom, d, depends on the displacements and the rotations at the nodes. These changes in degrees of freedom determine the deformations, ξ, of the elements. From the deformations, the stresses, ζ in the elements can be calculated. Once the stresses are known, the information about the external load is also available. Therefore, the three governing equations of the system are
Continuity Equation

$$\delta\xi = D[d]\delta d \tag{D.20}$$

Constitutive Equation

$$\zeta = S\xi \tag{D.21}$$

Equilibrium Equation

$$f = D^T\zeta \tag{D.22}$$

From the three governing equations, the external force at the nodes can be written as

$$f = (D[d])^T S\xi[d] \tag{D.23}$$

For simplification, we can write this equation as

$$f^{ext}[\lambda] = f^{int}[d] \tag{D.24}$$

where

$$f^{int}[d] = (D[d])^T S\xi[d]$$

$$f^{ext}[\lambda] = f$$

where λ is the load parameter. The load parameter is used to scale the load system. If $\lambda = 0$, it means the load is absent and on increasing the value of λ means an effective increase in the load.

$$f^{ext} = f = \lambda q$$

where q is the load that is scaled up and down by λ.
Equation (D.24) is highly non-linear in nature and the FEA software uses Newton-Raphson method to solve that equation. Newton-Raphson process evaluates the change in the degrees of freedom of the element with a small change in the load factor. It uses a process of iterative linearization of the the non-linear problem. Figure D.4 shows a Load Vs DOF plot that is exhibiting a non-linear behavior. An initial guess, x_0 for the solution is made. One solution that we know of is, that at $\lambda = 0$, d = 0. In the Load Vs DOF plot the red dot is the known solution. A local linearization at that point is made by the means of a tangent line and the next solution is looked at in the direct neighborhood of the red dot. So, for a small change in λ a corresponding change in d is found by local linearization. Now, to implement

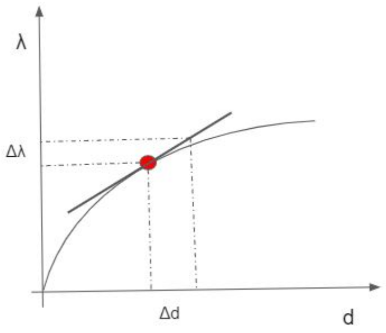

Figure D.4: A non-linear quadratic Loads Vs DOF plot

this analytically a formula for each approximation in terms of the previous one, i.e. x_{n+1} in terms of x_n is needed. The equation of the tangent line to the curve $y = f(x)$ at the point $(x_0, f(x_0))$ is

$$y - f(x_0) = f'(x_0)(x - x_0) \tag{D.25}$$

The tangent intersects the x-axis when $y = 0$ and $x = x_1$, now

$$-f(x_0) = f'(x_0)(x_1 - x_0) \tag{D.26}$$

Solving for $x_{(n+1)}$

$$x_{(n+1)} = x_n - \frac{f(x_n)}{f'(x_n)} \tag{D.27}$$

In this way, a solution is traced to a non-linear curve by means of small linearized steps. Linearization is nothing but differentiation. Coming back to our starting point, i.e. differentiating the equilibrium equation (D.24) w.r.t λ

$$\frac{df^{int}}{d\lambda} = \frac{df^{ext}}{d\lambda} \tag{D.28}$$

Since, it is known that f^{int} is dependent on the DOF, d

$$\frac{df^{int}}{dd}\frac{dd}{d\lambda} = \frac{df^{ext}}{d\lambda} \tag{D.29}$$

Defining K_t as a tangent stiffness matrix, where

$$K_t[d] = \frac{df^{int}}{dd} \tag{D.30}$$

therefore,

$$K_t[d]\frac{dd}{d\lambda} = \frac{df^{ext}}{d\lambda} \tag{D.31}$$

substituting the values of f^{int} from equation (D.24) in equation (D.31), we get

$$K_t = D^T S D + G \tag{D.32}$$

where

$$G = \sum_r \zeta_r^k \xi_{r,ij}^k$$

Interesting thing to note here is that the stiffness matrix K_t involves the stresses, ζ_r^k in the model and that is how the stresses induced in the model influences the structure stiffness.

Bibliography

[1] Singh A. “Investigation into the factors contributing to bicycle disc brake noise by Design of Experiments”. In: (2022).

[2] Harald Abendroth and Boris Wernitz. *The integrated test concept: Dyno-vehicle, performance-noise*. Tech. rep. SAE Technical Paper, 2000.

[3] A Akay, J Wickert, and Z Xu. “Investigating criteria for the onset of mode lock-in”. In: *Pittsburgh, Carnegie Mellon University, Internal Report* (1998).

[4] Adnan Akay. “Acoustics of friction”. In: *The Journal of the Acoustical Society of America* 111.4 (2002), pp. 1525–1548.

[5] R Allgaier et al. “Mode lock-in and friction modelling”. In: *WIT Transactions on Engineering Sciences* 24 (1970).

[6] F Wu-Bavouzet et al. “Stick-Slip: Wet Versus Dry”. In: *Journal of Adhesion - J ADHES* 83 (Aug. 2007). DOI: `10.1080/00218460701586178`.

[7] *Brake Pad Slots*. URL: `https://ricksfreeautorepairadvice.com/brake-pad-slots/`.

[8] Tomas Budinsky, Peter Brooks, and David Barton. “A new prototype system for automated suppression of disc brake squeal”. In: *Proceedings of the Institution of Mechanical Engineers, Part D: Journal of Automobile Engineering* 235.5 (2021), pp. 1423–1433.

[9] SN Chan, JE Mottershead, and MP Cartmell. “Parametric resonances at subcritical speeds in discs with rotating frictional loads”. In: *Proceedings of the Institution of Mechanical Engineers, Part C: Journal of Mechanical Engineering Science* 208.6 (1994), pp. 417–425.

[10] J.D. Fieldhouse and T.P. Newcomb. *An Investigation Into Disc Brake Squeal Using Holographic Interferometry*. Tech. rep. 3rd Int’l EAEC Conference on Vehicle Dynamics and Powertrain Engineering - EAEC Paper No. 91084, Strasbourg, 1991.

[11] *ICE TECHNOLOGIES*. URL: `https://bike.shimano.com/en-EU/technologies/component/details/ice-technologies.html`.

[12] P Ioannidis, Peter C Brooks, and DC Barton. “Drum brake contact analysis and its influence on squeal noise prediction”. In: *SAE paper* (2003), pp. 01–3348.

[13] NM Kinkaid, Olivier M O’Reilly, and Panayiotis Papadopoulos. “Automotive disc brake squeal”. In: *Journal of sound and vibration* 267.1 (2003), pp. 105–166.

[14] AM Lang, TP Newcomb, and PC Brooks. “Brake squeal-the influence of rotor geometry”. In: *PROCEEDINGS OF THE INSTITUTION OF MECHANICAL ENGINEERS. BRAKING OF ROAD VEHICLES. INTERNATIONAL CONFERENCE HELD 23-24 MARCH 1993 AT BIRDCAGE WALK, LONDON (PAPER NUMBER C444/016/93)*. 1993.

[15] HR Mills. *Brake squeak*. Institution of Automobile Engineers, 1938.

[16] Takashi Nakae et al. “Squeal and chatter phenomena generated in a mountain bike disc brake”. In: *Journal of Sound and Vibration* 330.10 (2011), pp. 2138–2149.

[17] Masaaki Nishlwakl et al. *Study on disc brake squeal*. Tech. rep. SAE Technical Paper, 1989.

[18] Soojin Park et al. “Brake-disc holes and slit shape design to improve heat dissipation performance and structural stability”. In: *Applied Sciences* 12.3 (2022), p. 1171.

[19] M Radeş. “Displays of Vibration Properties”. In: *Encyclopedia of Vibration, Pages 413-431* (2001).

[20] SK Rhee, PHS Tsang, and YS Wang. “Friction-induced noise and vibration of disc brakes”. In: *Wear* 133.1 (1989), pp. 39–45.

[21] M Triches Jr, SNY Gerges, and R Jordan. “Reduction of squeal noise from disc brake systems using constrained layer damping”. In: *Journal of the Brazilian Society of Mechanical Sciences and Engineering* 26 (2004), pp. 340–348.